Citation for final published version:

Maier, W. D. , Rasmussen, B., Fletcher, I. R., Godel, B., Barnes, S. J., Fisher, L. A., Yang, S. H., Huhma, H. and Lahaye, Y. 2015. Petrogenesis of the ∼2·77 Ga Monts de Cristal Complex, Gabon: Evidence for Direct Precipitation of Pt-arsenides from Basaltic Magma. Journal of Petrology 56 (7) , pp. 1285-1308. 10.1093/petrology/egv035

Publishers page: http://dx.doi.org/10.1093/petrology/egv035

Petrogenesis of the ~2.77 Ga Monts de Cristal Complex, Gabon: evidence for direct precipitation of Pt- arsenides from basaltic magma

WD Maier, School of Earth and Ocean Sciences, Cardiff University, UK (corresponding author)

B Rasmussen & I Fletcher, Curtin University, Australia

B Godel, SJ Barnes & LA Fisher CSIRO, Perth, Australia

Shenghong Yang, Department of Geosciences, University of Oulu, Finland

H Huhma & Y Lahaye, GTK, Espoo, Finland

Running title: Petrogenesis of the Monts de Cristal Complex, Gabon

ABSTRACT

The Monts de Cristal Complex of Gabon consists of several igneous bodies interpreted to be remnants of a tectonically dismembered, > 100km long and 1-3 km wide, ultramafic-mafic intrusion emplaced at 2765-2775 Ma. It is the most significant mafic-ultramafic layered complex yet identified on the Congo craton. The Complex consists largely of orthopyroxenite cumulates, with less abundant olivine-orthopyroxenites and norite, and rare harzburgites and dunites. Mineral compositions (Fo_{ol} 84, $Mg\#_{Opx}$ 85, An_{plag} 60-68, Cr/Fe chromite 1-1.45) and whole rock data suggest that the magma was a low-Ti basalt containing approximately 10% MgO and 0.5% TiO_2. Trace element and Rb-Sr and Sm-Nd isotope data indicate the presence of an enriched component, possibly derived from crustal contamination of a magma generated in the sub-lithospheric mantle. Most rocks show a highly unusual pattern of strong Pt enrichment (10-150 ppb) at low concentrations of Pd (1-15 ppb), Au (1-2 ppb), Cu (1-20 ppm), and S (<500 ppm) suggesting that, unlike in most other PGE rich intrusions globally, platinum in the Monts de Cristal Complex is not hosted in magmatic sulfides. Synchrotron X-ray fluorescence mapping revealed the location of buried small Pt particles, most of which are associated with As. We propose that this constitutes some of the strongest evidence yet in support of magmatic crystallization of a Pt-As phase from S undersaturated magma.

Keywords: Gabon; layered intrusion; platinum-group elements; Pt arsenide; synchrotron

INTRODUCTION

The Monts de Cristal (MdC) Complex, locally also referred to as the Kinguele Complex, is located in NW Gabon, some 70-150 km to the NE of Libreville, and ~50-100 km north of the Equator (Fig. 1a). It forms a tectonically dismembered intrusion, ~100 km in length and mostly ~1-3 km wide (Fig. 1b), constituting the largest mafic-ultramafic layered intrusion so far discovered on the Congo craton. In terms of its inferred shape and the observed lithologies, it bears some resemblance to the PGE mineralized Great Dyke of Zimbabwe. Based in part on these analogies, several companies have conducted exploration for chromite seams and PGE reefs in the MdC during the last decades. After initially obtaining promising exploration indicators, namely elevated Pt concentrations across most of the strike of the Complex, it was ultimately realized that the Pt is not associated with cumulus magmatic sulfide, in contrast to economic PGE reefs elsewhere. However, the strong enrichment of Pt relative to Pd in the MdC is of considerable petrological significance, in that it constitutes the most convincing case yet identified for direct precipitation of Pt phases from basaltic magma. In the present paper, we provide a description and compositional characterization of these unique Pt enriched rocks and suggest a model for their formation.

REVIEW OF PREVIOUS WORK

The first account of mafic rocks in the MdC area was published by Arsandaux (1912) who reported the presence of ophitic gabbros associated with charnockite to the south of Kinguele. Noritic massifs were first indicated in the Libreville Est geological map of 1959 (Aubague and Hausknecht, 1959), but reconnaissance mapping of the intrusion only began in the 1980s when the Direction Générale des Mines et de la Géologie du Gabon, in collaboration with the French Bureau de Recherches Géologiques et Minières, carried out a regional mineral assessment comprising airborne geophysical suveys and stream geochemistry over an area of ~100.000 km^2. This program identified Archaean granite-gneiss basement rocks containing banded iron formation, amphibolites as well as gabbronoritic intrusives. The presence of ultramafic intrusives was first indicated in the 1:200 000 Kango geological sheet (Kassa-Mombo et al., 1988). Mineral exploration activities initially focused on chromite, but no massive seams were found and the detrital chromite grains turned out to be too Fe- and Al-rich to be of economic interest (Campiglio et al., 1983). Reconnaissance geochronological work indicated an age of ~ 2.78 Ga (2777±83 Ma, Rb-Sr on whole rocks, 2783±77 Ma, Pb-Pb on whole rocks, Caen-Vachette et al., 1988).

In 2002, Southern Era Resources Limited started an exploration program for PGE in the MdC, comprising mapping, comprehensive stream sediment sampling, and soil sampling. Significant Pt anomalies closely associated with all blocks of the intrusion were delineated and a large number of outcrop samples were collected for high-precision geochemistry and geochronology (Maier, 2004). The exploration licence was acquired by Lonmin in 2005 which carried out extensive soil sampling at KG1, KG1 extension and KG3, and remapped some of the bodies (Prendergast, 2009). The company also drilled 15 diamond drill holes (13 holes at KG1 and two holes at KG3). In addition, a detailed magnetic-radiometric survey was conducted by Fugro Airborne Surveys in 2008.

ANALYTICAL METHODS

Whole rock and mineral chemistry

Seventy five outcrop samples were analysed for major and minor elements as well as a range of lithophile trace elements including Sr, Rb, Nb, Y, Zr, Ni, Cu, Zn, Co, Cr, Sc, V and REE using ICP-MS at Cardiff University, UK, after grinding to <75 μm in agate ring and ball mills. The concentrations of the PGE were determined using ICP-MS after nickel sulfide fire assay and tellurium co-precipitation, on 15 g aliquots. Full details of the analytical procedures used are given in McDonald and Viljoen (2006). The analytical procedure was validated by frequent analysis of reagent blank samples, replicate samples and reference materials (Electronic Appendix 1). All whole rock data are listed in Electronic Appendix 2, and average compositions of rocks types are given in Table 1. In addition to the outcrop samples, Lonmin analysed ~2000 samples from 13 drillcores for Pt, Pd and Au as well as selected major (Fe, Mg, Al, Ca), minor (Ti, Mn) and trace elements (Cr , Ni, Cu, Co, V, Zn, S, and Zr), at Genalysis, Johannesburg, using Pb-collection fire assay followed by mass spectrometry for Pt, Pd and Au, and ICP-OMS for a range of other major and trace elements. The Pt contents and the Pt/Pd ratios from the commercial lab show good overlap with the ICP-MS PGE data, suggesting the 2 methods have broadly similar accuracy (Maier, 2009).

In situ Sr isotope analyses of plagioclase were performed by Laser ablation ICP-MS using a Nu Plasma HR multi-collector inductively coupled plasma mass spectrometry (MC-ICP-MS) and a Photon Machine Analyte G2 laser microprobe at the Geological Survey of Finland in Espoo. Analytical details are given in Yang et al. (2013), and the complete data are provided in Electronic Appendix 3.

Whole rock Nd isotopes were also determined at GTK in Espoo. Analytical details are given in Huhma et al. (2012), and data for 5 samples are provided in Electronic Appendix 4.

The compositions of orthopyroxene, olivine, plagioclase and chromite were determined in 5 samples of (olivine)orthopyroxenite, 1 sample of norite, and 2 samples of gabbro from the KG1 and KG3 blocks (Electronic Appendix 5-8). The instrument used was a JEOL JXA-8200 electron microprobe at the University of Oulu, operated at an accelerating voltage of 15 kV and a beam current of 30 nA. The accuracy of analyses was monitored using reference material of similar composition. The reproducibility varied by less than 2 %.

Synchrotron X-ray fluorescence microscopy

X-ray fluorescence microscopy using synchrotron radiation is a highly effective technique for locating ultra-trace high-Z components, owing to the effective penetration of the x-ray beam and the fluoresced target x-rays through sample volumes. A protocol has been developed for searching for micron-scale precious metal (Au, PGE) enriched grains within geological materials (Ryan et al. 2014). X-ray fluorescence microscopy (XFM) was performed on the XFM beamline at the Australian Synchrotron in Melbourne (Paterson et al., 2011) using the Kirkpatrick Baez mirror microprobe end-station. This provides a monochromatic 2 µm beam-spot size for energies in the range 4-20 keV. Equipped with the Maia 384 detector array, the XFM beamline can acquire images at 2 µm resolution over areas of several square centimetres (Kirkham et al., 2010; Ryan et al., 2010a) with count rates of ~ 4-10 M/s and energy resolution of 300-400 eV. In this study, large area element maps were collected on 100 micrometer thickness polished thin sections backed by 1millimetre quartz glass slides with a beam energy of 18.5 keV, spot size of 2µm and a dwell times per pixel of 0.97 milli-second to locate areas where Pt-rich inclusions were observed. For each sub-area identified, additional maps were collected with longer dwell time (15.26 millisecond per pixel) to enhance the signal to noise ratio and improve further quantification. Each dataset was analysed with the GeoPIXE software suite which uses a fundamental parameters approach, with spectral deconvolution and imaging using the Dynamic Analysis method (Ryan, 2000; Ryan et al., 2010c) and a detailed model of Maia detector array efficiency (Ryan et al., 2010b). Data were fitted using a yield file which calculates the effects of X-ray absorption by the given matrix or mineral phase (Ryan, 2000). Element maps were produced after spectra were fitted and a dynamic analysis matrix file produced. Platinum abundance was measured using the Lα line. These maps were then interrogated to confirm the presence of Pt and identify associated elements and phases. It must be noted that this method samples potentially the entire 100 micrometer thickness of the section, and thus Pt may be sitting on a buried grain boundary even if it appears within a grain. The true nature of the grain location is difficult to resolve without milling down to the grain, but it is possible to further interrogate the spectra to gain a rough quantification of probable depth in the sample to assist with this. The correct identification of Pt has been confirmed by matching XFM maps collected using this methodology with Pt phases identified at the sample surface by optical microscopy in sulfide ore samples (Barnes et al., 2011), although as yet we have not identified any optically visible Pt phases in the Monts de Cristal samples. Identification of Pt phases in Monts de Cristal samples has been confirmed by high resolution PIXE imaging (Barnes et al., in prep).

Geochronology

Examination of orthopyroxenite samples Px12, Px39 and 1290 by scanning electron microscope revealed the presence of four U-Pb geochronometers: baddeleyite, zircon, zirconolite and monazite (Electronic Appendix 9). However, zircon grains appeared to have been affected by radiation damage and zirconolite was largely destroyed by secondary alteration, rendering both unsuitable for dating. Baddeleyite and monazite were viable for ion microprobe geochronology but the small size and limited number of grains constrain the data quality. Crystals of both minerals >10 μm in size were drilled from polished thin sections in ~3 mm platelets and mounted in 25 mm resin disks for ion microprobe (SHRIMP) analysis.

Baddeleyite was analysed using a ~0.15 nA O2- primary ion beam focused on a <10 µm spot. A chip of Phalaborwa (2060 Ma) baddeleyite was mounted with the samples for Pb/U calibration and as a monitor of Pb isotope data quality. Monazite analyses used a ~10 µm, 0.25 nA primary ion beam. Monazite reference samples (French, PD-95, z2234 and QMa28-1) were in a separate mount that was cleaned and Au-coated with the sample mount. Baddeleyite data acquisition and reduction followed the procedures of Wingate et al. (1998). Monazite procedures were those of Fletcher et al. (2010). Primary data reduction was performed using Squid-2 software (Ludwig, 2009), using "spot average" data for all ratios. Corrections to monazite data for matrix effects in Pb/U and Pb/Th, and a small correction for instrumental mass fractionation were applied.

STRUCTURE AND LITHOLOGIES

The MdC is largely hosted by Archaean basement rocks comprising granite-gneiss and greenstones. The basal contacts of the intrusions dip steeply towards the centres of the intrusive blocks (~80°) and are defined by aphanitic margins, grading inwards to medium-grained norite, orthopyroxenite and, less abundantly, harzburgite and dunite (Edou Minko et al., 2002). In addition, the Southern Era and Lonmin exploration programs discovered isolated anorthosite layers and several occurrences of ophitic gabbro, the latter located near the margins of the KG1 and KG3 blocks. All mafic-ultramafic rocks are generally poorly layered and lack distinct differentiation cycles. The norites appear to form lenses within the orthopyroxenites rather than distinct, laterally persistent, layers. In addition, norites appear to be relatively common towards the basal contact of the intrusions, e.g., at KG3 (drill core MPD 015) and at KG1 (drill cores MPO-03 and 04). Xenoliths of the country rocks, consisting mainly of feldspar-rich amphibolites as well as less abundant felsic fragments, have been intersected in several boreholes at the KG1 intrusive block.

The most comprehensive information on the geology of the Complex is available from KG1, where an extensive soil geochemical program was conducted (Prendergast, 2009). The location of the grab samples analysed by us, and some of the bore holes drilled by Lonmin in 2007-2008 are indicated in Fig. 2. The KG1 mafic-ultramafic body measures ~ 8 km by 2 km and appears to consist of two distinct blocks (Prendergast, 2009; Fig. 2). In the west and north, the intrusion is hosted by felsic gneisses and mafic schists interpreted to represent a granite-gneiss-greenstone terrane. Tonalitic to granodioritic granite gneiss containing intercalations of quartzite, amphibolite and ultramafic slivers occurs to the south and east of the body. Proterozoic clastic and chemical sedimentary rocks occur to the west of an inferred N-NE trending fault, 1-2 km west of KG1. Most contacts of the intrusion with its host rocks are tectonic (Prendergast, 2009), but the intrusive basal contact of the body has been intersected by drill cores MPD-03 and 04 (Fig. 2). This intrusive contact consists of a 1-2 m aphanitic rock interpreted as a chilled margin that grades to orthopyroxenite (Electronic Appendix 10). Based on the concordance of the strike of layering with the NW flank of the intrusion, Prendergast (2009) proposed that the intrusive contact strikes SW-NE and dips at ~60° to the SE, and that the total stratigraphic thickness is ~1700 m. The dip of layering in most of the remainder of the Complex remains unclear, due to weathering and paucity of layering.

The rocks of the KG1 block are mainly massive orthopyroxenites. Norites appear to be relatively abundant along the south-central margin, whereas olivine pyroxenite and occasional harzburgite predominantly occur in the east, consistent with elevated Ni values in soil sediment surveys. In drill core MPD-03 there is a ~ 400 m basal reversal expressed by a downward decrease in grain size together with an increase in modal plagioclase and biotite, relatively prevalent orthocumulate textures, several noritic intervals, occasional acicular textures, and enclaves of felsic melt rock. In another drill core (MPD-01), relatively fine grained orthopyroxenite overlying the floor contains xenoliths of amphibolite. All segments of the MdC intrusion are cut by abundant amphibolized plagioclase-clinopyroxene-phyric dolerites of unknown age.

PETROGRAPHY

The ultramafic rocks are mostly heteradcumulates or mesocumulates with between ~5 and 15% intercumulus material (Fig. 3a-c). Orthocumulates are less abundant and mainly confined to the stratigraphically lower portions of the intrusion. Considering the Archean age of the Complex, most rocks are remarkably unaltered. Minor to moderate serpentinization and chloritization is observed predominantly in the olivine-bearing lithologies. Orthopyroxene is mostly up to 2 mm in size, commonly of euhedral or subhedral habit (Fig. 3b-c), and aligned sub-parallel to the layering. Olivine forms anhedral grains up to 4 mm in width that can be moderately altered to serpentine and magnetite. Plagioclase occurs as either intercumulus, poikilitic or, in places, cumulus grains. In the orthopyroxenites, chromite tends to be rare, forming occasional clusters and chains of very small (< 0.01mm) euhedral and subhedral crystals included in orthopyroxene (Fig. 3d-e). Chromite is slightly more abundant in olivine pyroxenites, where grains tend to be larger (up to 0.1 mm) and may occur within, or interstitial to, orthopyroxene. Clinopyroxene is relatively rare as an interstitial phase (mostly < 1-2 modal%), but commonly forms exsolution lamellae and blebs in orthopyroxene. Phlogopite is a common accessory phase and may constitute up to 2 modal % in some samples. Hornblende, tremolite and actinolite are accessory phases, largely related to alteration. Sulfides form small grain aggregates up to about 20 microns in size mostly located on orthopyroxene grain boundaries and consist of pyrrhotite, pentlandite and chalcopyrite. Notably, many orthopyroxenes are distinctly zoned showing dark rims (Fig. 3c). Synchrotron X-ray fluorescence mapping has shown the rims to be Ti enriched. The absence of residual phases such as apatite, amphibole or K-feldspar implies that the last few percent of trapped liquid was completely expelled from the rock during heteradcumulate formation, at least at the scale of a thin section.

Norites consist mainly of subhedral orthopyroxene and intercumulus or cumulus plagioclase. The latter forms tabular subhedral crystals up to 4 mm in length (Fig. 3f). Clinopyroxene is intercumulus and phlogopite, quartz and alkali feldspar are accessory phases. Chromite is rare, occasionally occurring as clusters of very small grains included in orthopyroxene, similar to the orthopyroxenites. Based on the above observations, the crystallization sequence of the exposed portion of the Monts de Cristal intrusion is ol+cr – opx – opx+pl - opx+pl+cpx.

Gabbros are represented by just two samples, one from KG3 (sample Dy18), and the other from KG1 west (sample Hz3). The rocks have a medium-grained ophitic texture, containing tabular, elongated plagioclase (up to 1 mm long) and anhedral or subhedral clinopyroxene (up to 2 mm) (Fig. 3g-h). Olivine is a minor phase, forming mostly relatively small (<1mm) anhedral crystals, but occasionally they occur as larger grains up to 1 cm across. Magnetite forms anhedral aggregates reaching up to 1-5 modal %. Sulfides comprise mainly pyrrhotite and chalcopyrite that form very small trace phases.

The amphibolites are fine to medium grained rocks. Plagioclase forms subhedral tabular crystals up to 2 mm long and < 1 mm wide. Amphibole grains tend to be anhedral or, in some cases, subhedral, forming pseudomorphs of pyroxene. Some samples have granular textures and are finer grained, suggesting metamorphic recrystallisation.

MINERAL CHEMISTRY

In general, the analysed MdC samples show relatively limited mineral compositional variation compared to other layered intrusions. Olivine has mostly 75-84 Fo and 2400-3600 ppm Ni, with one sample having 4400 ppm Ni. These Ni contents are higher than those of olivines with equivalent Fo contents in most other layered intrusions (Fig. 4). Orthopyroxene has Mg# 0.78-0.85, 200-1000 ppm Ni, 0.4-0.7% Cr_2O_3, and up to 2% Al_2O_3. Cumulus plagioclase has An 67, whereas intercumulus plagioclase has An 60-68. Chromite contains around 40% Cr_2O_3, and has Cr/Fe ~ 1 to 1.4. Norites have approximately similar mineral compositions as the orthopyroxenites.

Two samples of fine-grained ophitic gabbro from the margins of the intrusion have slightly less magnesian clinopyroxene (Mg#0.77-0.8) than the orthopyroxenites and norites. Plagioclase (An63-67) is of similar composition as in the norites, but olivine in the gabbros is significantly more iron-rich (Fo57-58) than in the other lithologies.

WHOLE ROCK CHEMISTRY

Lithophile elements

Concentrations of Al_2O_3, TiO_2, Cr, and Ni are plotted vs MgO in Figure 5a-d. The MdC orthopyroxenites and norites have between 15 and 32% MgO, whereas the ophitic gabbros have between 8.5-9% MgO. The concentrations of the major and minor elements are mainly controlled by the modal proportions of orthopyroxene, olivine, and plagioclase. Based on the lever rule, it is estimated that the proportion of olivine to orthopyroxene may reach up to ~20%, consistent with petrographic data. The composition of the trapped melt cannot be well constrained, except for TiO_2 where a best fit line through the ultramafic rocks indicates TiO_2 levels in the trapped melt of around 0.5 wt%. REE patterns of most samples are fractionated (Electronic Appendix 11), showing relative enrichment in LREE over HREE, but Gd/Lu_N <1. Only a few samples show slight positive or negative Eu anomalies. Incompatible trace element patterns show marked enrichment in LILE, positive Th anomalies, and negative anomalies in Nb-Ta and P (Fig. 6), indicating the presence of an enriched component in the rocks.

Trace element contents in the two gabbro samples are more than 5 times those in the orthopyroxenites and norites. Together with their ophitic texture, this suggests that the samples approach liquid compositions, either frozen against the margin of the intrusion or emplaced as dykes or sills. The rocks have 47-48% SiO_2, 8.5% MgO, 12 % Fe_2O_3, 15% Al_2O_3, 0.7-0.8% TiO_2, 2% Na_2O and 0.1-0.2% K_2O (Table 1). They can thus be classified as Al-tholeiites. The multi-element patterns of the gabbros are much flatter and less fractionated than those of the orthopyroxenites and norites (Fig. 6). The two samples analysed have remarkably similar trace element patterns, considering that they were collected from two different intrusive blocks located > 50 km apart. The patterns show only subtle negative Nb-Ta anomalies, reminiscent of many Archean basalts (Barnes et al., 2012). Zirconium contents of the gabbros are ~50ppm, in the range of Yilgarn low-Ti basalts (Barnes et al., 2012), as are Cr and Ni contents (~400 and 200 ppm, respectively).

The amphibolite dykes also have relatively flat trace element patterns (Fig. 6h). The concentrations of most incompatible trace elements are significantly elevated relative to the orthopyroxenites and norites, by an order of magnitude. This is consistent with the amphibolites representing liquids. The shape of the multi-element patterns is broadly similar to those of the gabbros, except that the amphibolites have strong negative Sr anomalies and are relatively more enriched in LILE. Furthermore, the amphibolites have markedly higher total incompatible element concentrations than the gabbros.

Sulphur and chalcophile elements

The sulphur contents of the MdC cumulates are mostly < 100 ppm, consistent with the paucity of sulphides in the thin sections. Sulphur shows a weak positive correlation with TiO_2 (Fig. 7) suggesting that S behaved as an incompatible element during crystallization. We can place some constraints on the S content of the parent magma by means of the lever rule. The composition of the trapped melt can be delineated by a best fit line through the whole rock compositions of the least evolved orthopyroxenites. Assuming a TiO_2 content of ~0.4-0.5% for the liquid, as indicated by TiO_2-MgO relationships (Fig. 6b), the S content of the magma is between 100 and 300 ppm. As the S solubility of basaltic magmas at crustal pressure is on the order of 1000-2000 ppm (Mavrogenes and O'Neill, 1999), the MdC magma is likely strongly S undersaturated.

Copper contents of the MdC orthopyroxenites and ol-pyroxenites are mostly between 5 and 40 ppm (Electronic Appendix 12) showing a positive correlation with TiO_2. This indicates that Cu behaved as an incompatible element during fractionation, that the initial liquid (at 0.4-0.5% TiO_2) contained ~50-60 ppm Cu, and that the magma did not equilibrate with sulphide melt during fractionation.

For the noble metals, two datasets are available, one being based on 75 outcrop samples collected during the 2004 field season (Fig. 8), whereas the other is based on several 1000 drill core samples analysed during 2007-2008 (Fig. 9-10 and Electronic Appendix 13). The outcrop samples have up to 70 ppb Pt, but mostly <20 ppb Pd, <2ppb Au, <6 ppb Rh, <9 ppb Ru, and <2ppb Ir. As expected, the PGE contents in the drill cores cover a wider range extending to higher concentrations. The orthopyroxenites contain up to ~ 150 ppb Pt, 25 ppb Pd, 4 ppb Ir, 9 ppb Ru, 6 ppb Rh, and 3 ppb Au. With the exception of Pd and Au, the norites tend to contain lower PGE contents than the orthopyroxenites, i.e., up to ~ 20 ppb Pt, 15 ppb Pd, 1 ppb Ir, 3 ppb Ru, 2 ppb Rh, and 3 ppb Au. Pd and Au show weakly developed negative correlations with MgO (Fig. 8a-b), consistent with an incompatible behavior of the two noble metals. In contrast to Pd and Au, the other PGE (Pt, Rh and the IPGE) show positive correlations with MgO (Fig. 8c-f), indicating compatible behavior. Compatible behavior of the IPGE is not uncommon in mafic-ultramafic rocks (Barnes et al., 1985), but compatible behavior of Pt is rare (Park et al., 2013).

The drill core data show that the highest Pt values in unaltered rock are around 150 ppb (Fig. 9). These values occur in a specific layer that can be correlated laterally for several 100m. Soil geochemistry (Prendergast, 2009) suggests that beyond that, the layer either pinches out or is buried. Some strongly elevated Pt values are also observed within the 2-20m lateritic cover where Cu and Cr also show anomalously high values (Fig. 10). Notably, the highest Pt stream anomalies, in the centre of the KG1 body, do not correlate with elevated Pt in the soils. Possibly, the streams locally record residual Pt enrichment related to advanced weathering in a pronounced topographic gradient.

Of particular note are the high Pt/Pd ratios in the MdC (Pt/Pd mostly > 5), and the lack of correlation between Pt and Pd (Fig. 11b). This pattern is in marked variance to that observed in most other layered intrusions and mafic-ultramafic systems in general (Fiorentini et al., 2012; Maier et al., 2013). In contrast, Pt shows well defined positive correlations with the IPGE and Rh (Fig. 11a,c,d). Different blocks and sub-blocks of the MdC define distinct correlations, with KG1 having a relatively Rh and a relatively Pt enriched population, whereas KG1 extension, KG3 and KG4 each define distinct populations.

Highly anomalous Pd values have been found in a single example of a sulfide-bearing quartz vein associated with an amphibolite xenolith in drill core MPD 001 (Electronic Appendix 14). The rock contains up to 13.92 ppm Pd, 0.98% Cu, minor Au, 32 ppb Pt and < 10 ppb Rh and Ru.

The mantle normalized chalcophile element patterns for the orthopyroxenites and norites from all intrusive blocks (Electronic Appendix 15) show a progressive increase from Ir to Pt, followed by a decreasing trend through Pd and Au to Cu. The ophitic gabbros show very different patterns, with a progressive increase from Ir to Cu, and a small negative Au anomaly. The amphibolites have bowl-shaped patterns with strong PGE depletion relative to Cu and Ni.

Ratio plots of Cu/Pd and Cu/Zr (Fig. 12) allow an estimate of the fertility of the magmas. Cu/Pd of the orthopyroxenites and olivine pyroxenites is mostly around or below the level of the primitive mantle (PM), with outliers possibly explained by Pd mobility or localized and temporary sulfide saturation**.** Cu/Pd of the norites and gabbros tends to be slightly above mantle (~11000), reflecting moderate Pd depletion of the magma. The amphibolites have Cu/Pd significantly above mantle and thus crystallised from a PGE depleted magma that equilibrated with sulfide prior to solidification. Cu/Zr of most samples is 0.5-2, overlapping with, e.g., South African continental flood basalts (Maier et al., 2003), consistent with crystallization of the MdC rocks from a S undersaturated parent magma. Some samples have higher Cu/Zr. They could contain small amounts of cumulus sulfide, consistent with their low Cu/Pd ratios. The PGE depleted amphibolites have undepleted Cu/Zr suggesting that any sulfide that they equilibrated with was of low volume.

Sr and Nd isotopes

Strontium isotope data of plagioclase from two orthopyroxenites, one olivine pyroxenite and one gabbronorite from KG1 and KG3 show remarkable homogeneity between samples as well as between intrusive blocks (Electronic Appendix 3 and 16). The samples have $^{87}Sr/^{86}Sr_i$ 0.70255 - 0.70261 and positive εSr_T around +20, indicating an enriched component.

The four samples analysed for whole rock Nd isotope ratios (Electronic Appendix 4) show εNd_T -0.6 to 0.3, i.e. little variation between samples and intrusive blocks. As in the case of Sr isotopes, the Nd isotope data indicate the presence of an enriched component. The ophitic gabbro (DY18) has εNd +1.8, suggesting magma derivation from a depleted mantle source.

X-RAY FLUORESCENCE MICROSCOPY

X-ray fluorescence microscopy has provided added insight into the crystallization history of the MdC rocks, allowing location and identification of trace Pt rich phases. Figures 13 and 14 show two orthopyroxenite heteradcumulates containing cumulus orthopyroxene, approximately 5% plagioclase oikocrysts, minor intercumulus clinopyroxene, and trace chromite and olivine inclusions within orthopyroxene.

More than a hundred small Pt-rich phases have been found in the five samples mapped, with at least 12 in each sample, suggesting that such phases are quite common. The elevated Pt content across significant core intervals, e.g., 200m with 50-100 ppb Pt in drill core MPD 001 (Electronic Appendix 13) suggests a relatively homogenous distribution of these phases, which in turn suggests that there are few large grains. Such grains would be systematically under-sampled during petrographic analysis (Godel, 2013) and are unlikely to be detected by conventional methods.

The Pt phases located in the two samples reported in detail in this study are all less than 10 micrometres in size. The precise location in relation to the host grain boundary is difficult to determine precisely, owing to the unknown shape of the grain boundary in the third dimension, but it appears that all the Pt phases occur at or within a few tens of microns of the margins of orthopyroxene grains. Although the sample size is currently too small to be sure, none of the Pt phases was located within the Cr-zoned, chromite-bearing pyroxene grains, and their occurrence is apparently regardless of whether the host grain has a Ti-enriched rim. The great majority of grains so far identified fall at or close to the margins of orthopyroxene grains enclosed within plagioclase oikocrysts. This implies that the Pt phase or phases crystallised at the cumulus stage, but there is no association with chromite inclusions, as might have been predicted from the model of Finnigan et al. (2008).

The nature of the Pt-rich phases remains uncertain; all of the grains located so far lie beneath the surface of the host sample, and none have yet been observed optically or by SEM. Identification is therefore based on the element association obtained from the XFM data. About 50% of Pt grains show an association with As. For example, in sample Px21a there were 2 clusters of Pt grains, one associated with As, the other associated (but not co-located) with Ni and Cu. Approximate estimation of the depth of the grain in the sample in each case, based on variability of the apparent Pt peak height across the Maia detector array (Barnes et al., in preparation) indicates that in most cases Pt and As are co-located while the Ni-Cu peaks, attributed to sulfide phases, are slightly offset from Pt and As in 3D. The semi-quantified data indicate that in some, but not all, cases the visible coincident As and Pt spots on the map correspond approximately to sperrylite stoichiometry, $PtAs_2$. It is likely that at least some of the Pt grains are sperrylite. However, Pd is not detected by this technique, and neither is Te, although Bi is detectable and none of the observed grains show any Bi association. Further investigation is ongoing to increase the sample size of detected grains, and to locate these phases.

The small sulphide grains associated in some cases with the Pt rich phases could have formed in response to reaction of the PGM with S-saturated trapped liquid, or S-bearing hydrous fluid, although there is no evidence for magmatic hydrous phases within these particular samples. The great majority of the 100+ grains so far identified are therefore attributable to direct magmatic precipitation of sperrylite and/or other Pt-dominant phases, thought most likely to be Pt-Fe alloys.

GEOCHRONOLOGY

Twelve analyses were taken from six baddeleyite grains (Electronic Appendix 17 and 18). The data scatter in $^{206}Pb/U$, and most are apparently discordant but this is presumed to be due to grain orientation effects. They are closely grouped in $^{207}Pb/^{206}Pb$, giving a weighted mean age of 2775 ± 11 Ma. However, there is some excess scatter (MSWD = 2.6). Low-side culling makes little difference to MSWD and high-side culling reduces it to <0.7, implying overculling. Given the modest size of the data set, the variable precision of the $^{207}Pb/^{206}Pb$ data and the lack of clear justification for any data rejection, we use the most conservative option, retaining all data and hence taking the age of baddeleyite crystallization to be 2775 ± 11 Ma.

Ten analyses were obtained from four monazite grains (Electronic Appendix 19 and 20). The majority of the results are apparently 5-6% discordant, however the consistency of the offset from Concordia implies that this is due to a bias in Pb/U, possibly due to an unidentified matrix effect. The variability of minor element contents and lack of Y data make this impossible to assess, particularly for the one strongly discordant point, which is from a very high-Th sample.

The data appear to fall into three categories. There are three points that are close to Concordia and may be from concordant samples which have essentially identical ^{207}Pb/^{206}Pb. One other analysis matches this ^{207}Pb/^{206}Pb but is >10% discordant. This analysis had low $CePO_2^+$ counts and very high Th contents, suggesting that the spot inadvertently incorporated some huttonite. If this is true, the different (mixed) matrix might explain the apparent discordance. It is also possible that huttonite is metamict and has suffered “recent” Pb loss, and therefore that the analysed volume is genuinely discordant. These four analyses come from four distinct sample grains. The weighted mean ^{207}Pb/^{206}Pb dates for all four analyses is 2767 ± 7 Ma (including uncertainty propagated from the ^{207}Pb/^{206}Pb reference sample PD-95 that was used for mass fractionation correction), or 2766 ± 9 Ma if only the three most concordant analyses are used. A fifth analysis is ~2σ from the main cluster; incorporating it into the weighted mean gives 2765 ± 11 Ma, with only minor excess scatter (MSWD = 1.5).

The other data scatter along a trend that might be a mixing Discordia. The trend is too short and Pb/U too susceptible to matrix-induced errors for a lower intercept to be defined. However, it is almost inescapable to conclude that there has been at least one younger episode of monazite growth or recrystallization. Therefore the monazite gives a minimum age of 2765 ± 11 Ma for the orthopyroxenite, consistent with the baddeleyite date.

DISCUSSION

Parent magma composition

The composition of the MdC parent magma remains difficult to constrain. We have used two semi-quantitative approaches. First, we searched the literature to identify other examples of orthopyroxenite cumulates of broadly similar composition to the MdC, particularly those for which parent magma estimates are available. A relatively good compositional overlap exists with Bushveld orthopyroxenites (Fig. 6, and Electronic Appendix 11). We then simulated the crystallization of Bushveld B1 magma using PELE (Boudreau, 1999). A particularly good fit with the MdC rocks is provided by sample ECBV106 (Barnes et al., 2010: 10.07% MgO) at QFM and 100 bar. The simulation yields spinel as the first mineral to crystallize followed by olivine (Fo85), orthopyroxene (En86, after 10% crystallization) and then plagioclase (An69). Secondly, for one of our best characterized and least evolved samples (Px21) we determined modal proportions by point counting, and then subtracted the amount of MgO hosted by orthopyroxene from the whole rock composition. This method gave 8% MgO for the intercumulus component, but it needs to be borne in mind that the value is potentially affected by residual liquid percolation.

To get a rough idea about the concentration of incompatible minor and trace elements in the trapped melt, we have plotted best fit lines through the ultramafic rocks (Electronic Appendix 21) and recorded the trace element concentration at 10% MgO (TiO_2 0.4-0.5%, La ~8ppm, Ce ~10 ppm, Sm ~1-1.5 ppm, Th 2 ppm, Zr 40-60ppm, Ta 0.15 ppm, and Y 10-12ppm). Our data thus suggest that the MdC magma was a magnesian basalt with approximately 10% MgO, relatively low TiO_2 contents around 0.5 wt%, yet relatively high concentrations of other incompatible trace elements. TiO_2/La ratios are comparable to continental flood-type basalts with similar MgO contents, e.g., Ventersdorp and Dominion (Marsh et al., 1989, 1992). The whole rock trace element data can be modeled by up to 20% combined assimilation-fractionation-contamination (AFC) of magnesian basalt (having trace element contents assumed to be 4x primitive mantle, i.e. equivalent to ~25% partial mantle melting) with a 17% partial melt of MdC country rock granite (average of samples GRA 2W and GRA 2X, Electronic Appendix 2). The composition of the granitic partial melt was calculated by assuming restite modal proportions determined in melting experiments of biotite gneiss at 875° and 3kbar (Patino Douce and Beard, 1995), and D values summarized in Rollinson (2013) (Fig. 15). However, as the model contains a large number of variables, other interpretations are possible, including a magma source in the metasomatised mantle.

The Nd and Sr isotope data are broadly consistent with the interpretations from the trace element data. Assuming that the host granites had Sr_i of 0.7013 at 3120±67Ma (Rb/Sr whole rock method, Caen Vachette et al., 1988), and εNd 0.2 (i.e., approximately $CHUR_T$), and that the MdC magma was a magnesian basalt with 4x PM levels of Rb, Sr, Sm and Nd (Sun and McDonough, 1989), Sr_i 0.701, and εNd 2,1 (DM, De Paolo 1981), the MdC samples (Sr_i 0.70255-0.70261, εNd 0.3 to -0.6) can be modeled by 10-15% bulk contamination with host granite. Unfortunately, Caen Vachette et al. (1988) do not provide detailed information on sampling sites or trace element geochemistry, and their Rb-Sr dates have large uncertainties, which renders the above modeling semi-quantitative at best. To improve the reliability of the model, high-precision geochronology, isotope geochemistry and trace element data of the host granites are required.

The two ophitic gabbroic samples cannot represent the parent magma to the orthopyroxenites and norites, as the gabbros have distinctly less fractionated trace element patterns and less enriched Nd isotope signatures, as well as depleted PGE contents (Cu/Pd >7000). Whether the gabbros do indeed belong to the same magmatic event as the remainder of the MdC cumulates needs to be confirmed by dating.

Nature of PGE enrichment and PGE host phases

The Pd levels of most MdC ultramafic samples can be modeled by assuming that the rocks contain 10-30% trapped liquid (broadly consistent with petrography) with 20-25 ppb Pd. Such levels are at the upper end of Pd contents in global basalts (Fiorentini et al., 2010; Maier et al., 2013). Other examples of Pd rich basalts include Finnish 2.45 Ga tholeiitic dykes having up to 30-35 ppb (Guo et al., 2012), and Svecofennian basalts reaching 25 ppb (Barnes et al., 2009).

In contrast to Pd, the measured Pt contents of the MdC cumulates are far too high to be explained by a trapped liquid component. Our global database indicates that basaltic magmas may contain up to ~20 ppb Pt (Maier et al., 2013). A 30% trapped liquid component could thus account for no more than 6-7 ppb Pt. Hydrothermal introduction of Pt or removal of Pd and S after crystallization is considered unlikely, in view of the relatively homogenous nature of the PGE contents in the MdC along ~100km strike, and the generally unaltered nature of the rocks. Localized mobility of Pd is indicated by the development of vein-style mineralization, but this is extremely rare and closely associated with amphibolite xenoliths.

A more likely scenario is that the MdC magma had Pt contents in the range of other basalts (15-20 ppb), but reached Pt (or $PtAs_2$) saturation prior to sulfide saturation. This model is consistent with the synchrotron XFM data reported above and the low S contents of the MdC rocks (Fig. 7). Compatible behavior of Pt has previously been reported from other basaltic suites, including the Pual ridge (Park et al., 2012), where it was assigned to precipitation of Pt alloys.

As platinum shows well defined positive correlations with Ir, and to a lesser extent Ru and Rh (Fig. 11), these metals also appear to have been compatible during fractionation. Compatibility of IPGE in mafic-ultramafic rocks has been described in many igneous suites (Barnes et al., 1985, Puchtel and Humayun, 2001). From a crystal-chemical point of view, the IPGEs could be hosted by orthopyroxene and olivine, substituted for Mg in octahedral coordination, which has been shown to be the case for Ru, Rh and Ir in olivine (Brenan et al., 2003; 2005). Several studies have proposed that in mafic-ultramafic rocks the IPGE are mainly hosted by Os-Ir-Ru alloys and PGM (e.g., Peck and Keays, 1990), but as yet no IPGE enriched PGM could be identified in the MdC. Another possible host for the IPGE is chromite (Locmelis et al., 2011; Pagé et al., 2012), but chromite is rare in the MdC and thus unlikely to control IPGE distributions, at least in the form of solid solution. Some of the IPGE and Rh could be hosted in Pt alloys. For example, Pt alloys described by Garuti et al. (2002) have approximately 80% Pt, and 1-2% Ir, Ru, and Rh. However, in the MdC we do not see any detectable IPGE associated with the As phases, or anywhere else.

Factors controlling Pt saturation

PGE levels in basaltic magmas depend largely on the solubility of sulfide liquid, platinum-group minerals and PGE alloy during mantle melting and fractional crystallization in the crust. Small to medium degree (<10-20%) melts of asthenospheric mantle are saturated in sulfide (Barnes et al., 1985; Rehkämper et al., 1999; Mungall and Brenan, 2014) and thus depleted in all PGE. Upon dissolution of the mantle sulfides at larger degrees of melting, the concentrations of the individual PGE in the magma depend on whether sulfide is the main PGE host phase or whether, in addition, any PGM or PGE alloy is stable. Palladium is only controlled by sulfide and thus large degree mantle melts such as komatiites have Pd levels 2-3 times that of the primitive mantle (Fiorentini et al., 2013). Platinum levels additionally depend on whether Pt alloy is stable, which in turn is controlled by T, fO_2 and depth of melting (Mungall and Brenan, 2014). At relatively low pressure, Pt alloy is stable even at large degree melting, resulting in sub-chondritic Pt/Pd ratios in most asthenospheric mantle magmas (e.g., MORB and komatiites). Increased temperature, fO_2 and melting depth enhance Pt alloy solubility (Borisov and Palme, 1997; Fortenfant et al., 2003; Mungall and Brenan, 2014) leading to a decrease in the bulk partition coefficient of Pt. This should result in relatively high Pt/Pd in the melt, perhaps approaching the chondritic ratio as observed in Bushveld magmas. However, it is notable that global mantle melts mostly show Pt contents between 10-15 ppb (Maier et al., 2009; Fiorentini et al., 2010), with very few examples of higher values that might be expected in large degree melts generated at high pressure. This is likely due to the fact that the Pt levels of the magmas are capped by decreasing Pt solubility during magma ascent resulting in the precipitation of Pt alloys or PGM.

Enigmatically, the empirical data indicate much higher Pt solubilities in mafic magmas (10-15 ppb) than the available experimental data. Thus, Ertel et al. (1999) show that Pt solubility in basalt is as low as 3 ppb. Borisov and Palme (1997) proposed higher values, around 15 ppb, but their experiments probably overestimate the Pt solubility, as that work involved bulk analyses in which samples may have been contaminated with undissolved Pt particles. The mismatch between the natural magmas and the experimental data suggests that either the solubility model is wrong, or that other factors play a role. The experiments of Ertel et al. (1999) and Borisov and Palme (1997) were conducted on synthetic basalts which contained no Fe or S. Fe addition should result in the formation of Pt alloys and thus relatively lower Pt solubility (Borisov and Palme, 2000). However, Laurenz et al. (2013) have shown that the presence of sulfur in magmas significantly increases Pd and Ru solubility, and Mungall and Brenan (2014) have suggested a similar effect on Pt.

Of particular interest is the origin of the Pt enriched layer of the MdC (Fig. 10, and Electronic Appendix 13). The Pt rich samples are heteradcumulates that largely lack chromite and olivine. They have the highest Mg#, i.e., are the least evolved, but in terms of petrography, isotopes and incompatible trace element ratios they are compositionally indistinguishable from the other rocks. Due to the small size of the Pt phases located, gravitational concentration from convecting magma seems unlikely, unless the Pt phases nucleated on the surface of cumulus orthopyroxene grains and were mechanically concentrated with them. The Pt solubility could have been temporarily lowered due to reduction of the magma in response to contamination, but not only would this potentially have triggered sulfide saturation (Tomkins et al., 2012), but it is also inconsistent with the V contents of the rocks; The experimental data of Toplis and Corgne (1992) have shown that partitioning of V into pyroxene increases with falling O fugacity. Thus, one would expect an increase in V to accompany the Pt enrichment, contrary to the observations from the drillcore data that show inflections towards low V contents in the Pt rich layer. Furthermore, there is no lithological evidence such as country rock xenoliths that could suggest local magma contamination in the Pt enriched horizon. Localised reduction due to chromite crystallization (Finnigan et al., 2008) can be ruled out because the most Pt rich samples are chromite poor, and no Pt phases were observed by XFM mapping in contact with chromite grains. The available evidence suggests that the formation of the Pt enriched layer is related to magma replenishment with relatively unevolved magma, consistent with a subtle increase in Mg# and a decrease in V and Ti of the rocks.

An additional factor suggested by our observations is that arsenic plays a role in the stability of magmatic Pt phases. The evidence for primary precipitation of Pt-As rich phases, thought to be sperrylite, suggest that the key factor may be the magma exceeding the solubility product for sperrylite. If Pt is dissolved in the magma as PtS, as implied by the experimental data of Mungall and Brenan (2014), then the following reaction may be operating:

$$PtS(melt) + FeAs_2(melt) = PtAs_2(solid) + FeS(melt)$$

with the reaction being driven by the increasing activity coefficient of PtS with falling temperature along a given fO_2 buffer implied by the Mungall and Brenan experiments. This conjecture requires testing by investigation of solution properties of Pt in the presence of As in silicate melts, which are currently unknown. The divergence of Pt/Pd ratio noted in a number of layered intrusions and mafic lava suites (e.g., Stillwater, Keays et al., 2012; Deccan Trap lavas, Keays and Lightfoot, 2010) may be explained by preferential fractionation of magmatic Pt arsenides.

Unfortunately, no arsenic data are available to evaluate whether the elevated Pt contents in the MdC rocks could be due to unusually high As concentrations in the magma. However, assuming that all of the Pt occurs as $PtAs_2$, with overall Pt levels at ~20-150 ppb, this would require ~15-100 ppb As for charge balance. This is in the range of As contents reported by Jenner and O’Neill (2012) for MORB in the 8-10 wt% MgO range (~125 ppb As). Hence, the required As contents implied by the Pt contents of the rocks are not exceptional, adding support to the notion that Pt-arsenide might be more significant in S-poor rocks than previously supposed (J Brenan, written comment, Feb. 2015).

CONCLUSIONS

The Monts de Cristal Complex of Gabon forms a large layered intrusion, approximately 100km long and 1-3 km wide. It consists predominantly of orthopyroxenite that crystallised from a low-Ti basalt with approximately 10% MgO. The Complex is characterised by strong enrichment in Pt (up to 150 ppb) relative to Pd (<20 ppb) and other chalcophile elements and sulphur. X-Ray fluorescence microscopy has identified numerous small (<10 micrometers) Pt rich phases, mostly arsenides. This is interpreted to indicate precipitation of Pt-arsenides from S undersaturated magma, constituting some of the best evidence yet for direct crystallization of platinum- group minerals from basaltic magma.

ACKNOWLEDGEMENTS

We thank Sari Forss for producing thin sections, Leena Järvinen and Arto Pulkkinen for assistance with Sm-Nd isotope analysis, and Chris Ryan, Martin de Jonge and Daryl Howard for assistance and support in the XFM mapping component of this research, which was undertaken on the X-Ray Fluorescence Microscopy (XFM) beamline at the Australian Synchrotron, Victoria, Australia (AS grant 6618 to Godel, Barnes and Maier). C Li and J-W Park engaged in helpful discussions on S and Pt saturation. Lonmin is thanked for granting permission to publish the findings of our research and the geochemical data on the drill cores. Martin Prendergast allowed the use of his field map in Fig. 2. Discussions with Sarah-Jane Barnes and constructive reviews by Chusi Li and James Brenan helped to improve the manuscript significantly. This is an output from the CSIRO Minerals Down Under National Research Flagship.

REFERENCES

Arsandaux, H. (1912). Sur la presence au Gabon de roches appartenant a la serie de la charnockite. *Comptes Rendus Academie Sciences*, Paris, **154**, 896-898.

Aubague. M. & Hausknecht, J.J. (1959). *Carte geologique de reconnaissance au l/500 000, feuille Libreville Est. Carte et notice explicative*. Direction des Mines et de la Geologie de I’AEF, Brazzaville, Congo, 34p.

Ballhaus, C., Berry, R.F. & Green, D.H. (1991). High pressure experimental calibration of the olivine-orthopyroxene-spinel oxygen geobarometer: implications for the oxidation state of the upper mantle. *Contributions to Mineralogy and Petrology* **107**, pp 27-40

Barnes, Sarah-Jane & Maier, W.D. (1999). *The fractionation of Ni, Cu and the noble metals in silicate and sulphide liquids*, in Keays, R.R., Lesher, C.M., Lightfoot, P.C. and Farrow, C.E.G., eds., *Dynamic processes in magmatic ore deposits and their application to mineral exploration*: Geological Association Canada, Short Course Notes, **13**, 69-106.

Barnes, Sarah-Jane, Naldrett, A.J. & Gorton, M.P. (1985). The origin of the fractionation of platinum-group elements in terrestrial magmas. *Chemical Geology* **53**, 303-323.

Barnes, Sarah-Jane, Maier, W.D. & Curl, E.A. (2010). Composition of the Marginal rocks aand sills of the Rustenburg layered suite, Bushveld Complex, South Africa: Implications for the formation of platinum-group element deposits. *Economic Geology* **105**, 1491-1511.

Barnes, S.J. (2007). Cotectic precipitation of olivine and sulfide liquid from komatiite magma and the origin of komatiite-hosted disseminated nickel sulfide mineralization at Mount Keith and Yakabindie, Western Australia. *Economic Geology* **106**, 298-304.

Barnes, S.J. & Naldrett A.J. (1984). Geochemistry of the J-M Reef of the Stillwater Complex, Minneapolis Adit area II. Slicate Mineral Chemistry and Petrogenesis. *Journal of Petrology*, **27**, 791-825.

Barnes, S.J., Makkonen, H.V., Dowling, S.E., Hill, R.E.T. & Peltonen, P. (2009). The 1.88 Ga Kotalahti and Vammala nickel belts, Finland: geochemistry of the mafic and ultramafic metavolcanic rocks. *Bulletin of the Geological Society of Finland* **81**, 103–141.

Barnes, S.J., Osborne, G.A., Cook, D., Barnes, L., Maier, W.D. & Godel, B. (2011), The Santa Rita Nickel sulfide deposit in the Fazenda Mirabela Intrusion, Bahia, Brazil: Geology, sulfide geochemistry and genesis. *Economic Geology* **106**, 1083-1110.

Barnes, S. J., Van Kranendonk, M. J., and Sonntag, I., 2012, Geochemistry and tectonic setting of basalts from the Eastern Goldfields Superterrane: *Australian Journal of Earth Sciences* **59**, 707-735.

Borisov, A. & Palme, H. (1997), Experimental determination of the solubility of platinum in silicate melts. *Geochimica et Cosmochimica Acta* **20**, 4349-4357.

Borisov A., Palme H. (2000) Solubilities of noble metals in Fe-containing silicate melts as derived from experiments in Fe-free system. American Mineralogist. 85 (11-12), pp. 1665-1673

Boudreau, A.E. (1999), PELE-a version of the MELTS software programme for the PC platform. *Computers and Geosciences* **25**, 201-203.

Bowles, J.F.W., Prichard, H.M., Suarez, S. & Fisher, P.C. (2013). The first report of PGM in magnetite-bearing gabbro, Freetown layered complex, Sierra Leone: Occurrences and genesis. *Canadian Mineralogist* **51**, 455-473.

Brenan J. M., McDonough W. F. and Dalpe´ C. (2003) Experimental constraints on the partitioning of rhenium and some platinum-group elements between olivine and silicate melt. *Earth Planet. Sci. Lett*. **212**, 135–150.

Brenan J. M., McDonough W. F. and Ash R. (2005) An experimental study of the solubility and partitioning of iridium, osmium and gold between olivine and silicate melt. *Earth Planet. Sci. Lett*. **237**, 855–872.

Caen-Vachette, M., Vialette, Y., Basset, J.P. & Vidal, P. (1988). Apport de la geochronologie isotopique a la connaissance de la geologic gabonaise. *Chronique Recherche Miniere* **491**, 35-53.

Campbell, I. H. & Griffiths, R. W. (1992). The changing nature of mantle hotspots through time: implications for the chemical evolution of the mantle. *Journal of Geology* **92**, 497-523.

Campiglio, C. (1987). *Perspectives sur la recherche de platinoides dans le complexe des Monts de Cristal, Gabon*. In: Rapport d'Execution de la Convention Concernant la Cellule d'orientation de I'lnventaire Minier Gabonais, 1986-1987. Armines-CGGM, France, 31-36.

Campiglio, C., Marion, C. & Vannier, M. (1983). *Le complexe mafique-ultramafique de M'Bilan. Etude des premiers echantillons de roches et de concentres alluvionnaires*. In: Annexes, Rapport Cellule d'orientation de I'lnventaire Minier, CGGM. Direction des Mines et de la Geologie Miniere, Libreville, Gabon, 22p.

Chevalier, L., Makanga, J.F. & Thomas, R.J. (2002). *Carte geologique de la Republique Gabonaise. Notice explicative*. Council for Geoscience, Pretoria, 195p.

Creighton, S., Stachel, T., Eichenberg, D. & Luth, R.W. (2010). Oxidation state of the lithospheric mantle beneath Diavik diamond mine, central Slave craton, NWT, Canada. *Contributions to Mineralogy and Petrology* **159**, 645-657.

DePaolo, D.J. (1981). Neodymium isotopes in the Colorado Front Range and crust-mantle evolution in the Proterozoic. *Nature* **291**, 684–687.

Edou-Minko, A., Grandin, G. & Campiglio, C. (2002). Petrologie et geomorphologie dans la region de Kango, Gabon: un grand dyke ultramafique-mafique archeen. *Journal of African Earth Sciences* **32**, 899-918.

Ertel W., O'Neill H., St C., Sylvester P. J. and Dingwell D. B. (1999) Solubilities of Pt and Rh in a haplobasaltic melt at 1300 °C. *Geochim. Cosmochim. Acta* **63**, 2439–2449.

Finnigan, C.S., Brenan, J.M., Mungall, J.E. & McDonough, W.F. (2008). Experiments and Models Bearing on the Role of Chromite as a Collector of Platinum Group Minerals by Local Reduction. *Journal of Petrology* **49**, 1647-1665.

Fiorentini ML, Barnes SJ, Lesher CM, Heggie, GJ, Keays RR, Burnham OM (2010) Platinum Group Element Geochemistry of Mineralized and nonmineralized Komatiites and Basalts. *Economic Geology*, **105**, 795-823.

Fiorentini, M.L., Barnes, S.J., Maier, W.D. & Heggie, G.J. (2012). Global variability in the PGE contents of komatiites, *Journal of Petrology* **52**, 82-112.

Fletcher, I.R., McNaughton, N.J., Davis, W.J., Rasmussen, B., 2010. Matrix effects and calibration limitations in ion probe U–Pb and Th–Pb dating of monazite. *Chemical Geology* **270**, 31–44.

Fortenfant, S.S., Gunther, D., Dingwell, D.B. & Rubie, D.C. (2003). Temperature dependence of Pt and Rh solubilities in a haplobasaltic melt. *Geochimica et Cosmochimica Acta* **67**, 123-131.

Garuti, G., Pushkarev, E.V. & Zaccarini, F. (2002). Composition and paragenesis of Pt alloys from chromitites of the Uralian-Alaskan-type Kytlym and Uktus complexes, northern and central Urals, Russia. *Canadian Mineralogist* **40**, 1127-1146.

Godel , B. (2013). High-Resolution X-Ray Computed Tomography and Its Application to Ore Deposits: From Data Acquisition to Quantitative Three-Dimensional Measurements with Case Studies from Ni-Cu-PGE Deposits. *Economic Geology* **108**, 2005-2019.

Harris, C., Pronost, J.J.M., Ashwal, L.D. & Cawthorn, R.G. (2004). Oxygen and hydrogen isotope stratigraphy of the Rustenburg layered suite, Bushveld Complex: constraints on crustal contamination. *Journal of Petrology* **46,** 579–601.

Huhma, H., Kontinen, A., Mikkola, P., halkoaho, T., Hokkanen, T., Hölttä, P., Juopperi, H., Konnunaho, J., Luukkonen, E., Mutanen, T., Peltonen, P., Pietikäinen, K., Pulkkinen, A., 2012. Sm–Nd results on the Archean crust in Finland. In: Hölttä, P. (Ed.), *The Archean of the Karelia Province in Finland*. Geological Survey of Finland, Special Paper 54, pp. 176–213.

Irvine, T.N. (1970). *Crystallization sequences in magmas of the Muskox intrusion and some other layered intrusions*. Geological Society of South Africa, Special Publication **1,** 441-476.

Irvine, T.N. (1980). *Magmatic infiltration metasomatism, double-diffusive fractional crystallisation, and adcumulus growth in the Muskox Intrusion and other layered intrusions*. In: R.B. Hargraves (Editor), Physics of Magmatic Processes. Princeton University Press, Princeton, N.J., 325-383.

Jacobsen, S.B. & Wasserburg, G.J. (1980). Sm-Nd isotopic evolution of chondrites. *Earth and Planetary Science Letters* **50**, 139–155.

Kassa-Mombo, C., Minko-Bidza, V., Mikhailoff, N., Greenish, T., Devos, W., Boldrachi, R., Degroote, V., Bonnot, H., Adlof, L., Mabiala, R., Melchior, A. & Abeme, M.J. (1988). Apport de I’inventaire aux connaissances geologiques et minieres des feuilles a l/200.000 de Libreville, Kango et Lambarene (Gabon). *Chronique Recherche Miniere* **491**, 105-124.

Keays, R.R., Lightfoot, 2010. Crustal sulfur is required to form magmatic Ni-Cu sulfide deposits; evidence from chalcophile element signatures of Siberian and Deccan Trap basalts. *Mineralium Deposita*, **45**, 241.

Keays, R.R., Lightfoot, P.C., Hamlyn, P.R., 2012. Sulfide saturation history of the Stillwater Complex, Montana: chemostratigraphic variation in platinum group elements. *Mineralium Deposita,* **47**, 151-173.

Kirkham, R., Dunn, P. A., Kucziewski, A., Siddons, D. P., Dodanwela, R., Moorhead, G., Ryan, C. G., De Geronimo, G., Beuttenmuller, R., Pinelli, D., Pfeffer, M., Davey, P., Jensen, M., Paterson, D., de Jonge, M. D., Kusel, M. & McKinlay, J. (2010). *The Maia Spectroscopy Detector System: Engineering for Integrated Pulse Capture, Low-Latency Scanning and Real-Time Processing*. AIP Conference Series, **1234**, 240-243.

Laurenz V, Fonseca ROC, Ballhaus C, Jochum KP, Heuser A, Sylvester PJ (2013) The solubility of palladium and ruthenium in picritic melts: 2. The effect of sulfur. *Geochim. Cosmochim. Acta*, **108**, 172-183

Li, C. & Ripley, E.M. (2009). Sulphur contents at sulfide-liquid or anhydrite saturation in silicate melts: empirical equations and example applications. *Economic Geology* **104**, 405-412.

Lightfoot, P.C. & Naldrett, A.J. (1983). The geology of the Tabankulu section of the Insizwa Complex, Transkei, southern Africa, with reference to the nickel sulphide potential. *Transactions of the Geological Society of South Africa*, **86**, 69–187.

Lightfoot, P.C., Naldrett, A.J. & Hawkesworth, C.J. (1984). The geology and geochemistry of the Waterfall Gorge Section of the Insizwa Complex with particular reference to the origin of the nickel sulphide deposits. *Economic Geology*, **79**, 1857–1879.

Locmelis, M., Pearson, N.J., Barnes, S.J. & Fiorentini, M.I. (2011). Ruthenium in komatiitic chromite. *Geochimica et Cosmochimica Acta* **75**, 3645-3661.

Ludwig, K.R. (2003). *User's Manual for Isoplot/Ex version 3.00–A Geochronology Toolkit for Microsoft Excel, No. 4* - Berkeley Geochronological Center, Special Publication

Maier WD (2004). Monts de Cristal PGE project. Internal Report 2, SouthernEra Resources Ltd.

Maier WD (2009). Report on PGE reef potential of the Monts de Cristal PGE project, Gabon, Lonmin Plc

Maier, W.D. & Eales, H.V. (1997). *Correlation within the UG2–Merensky Reef interval of the Western Bushveld Complex, based on geochemical, mineralogical and petrological data*. Geological Survey of South Africa Bulletin **120**, 56 p.

Maier, W.D., Groves, D.I. (2012). Temporal and spatial controls on the formation of magmatic PGE and Ni-Cu deposits. *Mineralium Deposita* **46**, 841-857.

Maier, W.D., Barnes, S.-J. & Marsh, J.S. (2003). The concentrations of the noble metals in Southern African flood-type basalts and MORB: implications for petrogenesis and sulphide exploration. *Contributions to Mineralogy and Petrology* **146**, 44-61.

Maier, W.D., Gomwe, T., Barnes, S.-J., Li, C. & Theart, H. (2004). Platinum-group elements in the Uitkomst Complex, South Africa. *Economic Geology* **99**, 499-516.

Maier, W.D., Barnes, S.-J. & Groves, D.I. (2013). The Bushveld Complex, South Africa: formation of platinum– palladium, chrome- and vanadium-rich layers via hydrodynamic sorting of a mobilized cumulate slurry in a large, relatively slowly cooling, subsiding magma chamber. *Mineralium Deposita* **48**, 1–56.

Marsh JS, Bowen MP, Rogers NW, Bowen TB (1989) Volcanic rocks of the Witwatersrand Triad, South Africa, I: Petrogenesis of mafic and felsic rocks of the Dominion Group. *Precambrian Research* 44, 39–65

Marsh JS, Bowen MP, Rogers NW, Bowen TB (1992) Petrogenesis of Late Archean flood-type basic lavas from the Klipriviersberg group, Ventersdorp Supergroup, South Africa. *Journal of Petrology* **33**, 817– 847

Martin, H., Smithies, R.H., Rapp, R., Moyen, J.-F. & Champion, O. (2005). An overview of adakite, tonalite–trondhjemite–granodiorite (TTG), and sanukitoid: relationships and some implications for crustal evolution. *Lithos* **79**, 1–24.

Mavrogenes, J. A. & O’Neill, H.St.C. (1999). The relative effects of pressure, temperature and oxygen fugacity on the solubility of sulfide in mafic magmas. *Geochimica et Cosmochimica Acta* **63**, 1173–1180.

McDonald, I. & Viljoen, K.S. (2006). Platinum-group elemeent geochemistry of mantle eclogites: a reconnaissance study of xenoliths from the Orapa kimberlite, Botswana. *Transactions Institution Mining and Metallurgy* **115**, 81-93.

McDonough, W.F. & Sun, S.-s. (1995). The composition of the Earth. *Chemical Geology* **120**, 223-253.

McInnes, B.I.A., McBride, J.S., Evans, N.J., Lambert, D.D. & Andrew, A.S. (1999). Osmium isotope constraints on metal recycling in subduction zones. *Science* **286**, 512-516.

Merkle, R.K.W. (1992). Platinum-group minerals in the middle group of chromitite layers at Marikana, western Bushveld Complex: indications for collection mechanisms and postmagmatic modification. *Canadian Journal of Earth Sciences* **29**, 209-221.

Müller, W., Shelley, M., Miller, P. & Broude, S. (2009). Initial performance metrics of a new custom-designed ArF excimer LA-ICPMS system coupled to a two-volume laser-ablation cell. *Journal Anal Atom Spectrom* **24,** 209–214.

Mungall, J.E. & Brenan, J.M. (2014). Partitioning of platinum-group elements and Au between sulfide liquid and basalt and the origins of mantle-crust fractionation of the chalcophile elements. *Geochimica et Cosmochimica Acta* **125**, 265–289.

Nebel, O., Scherer, E.E. & Mezger, K. (2011). Evaluation of the ^{87}Rb decay constant by age comparison against the U–Pb system. *Earth and Planetary Science Letters* **301,** 1–8.

Pagé, P., Barnes, S.-J., Bédard, J.H. & Zientek, M.L. (2012). In situ determination of Os, Ir, and Ru in chromites formed from komatiite, tholeiite and boninite magmas: implications for chromite control of Os, Ir and Ru during partial melting and crystal fractionation. *Chemical Geology* **302–303,** 3–15.

Park, J.-W., Campbell, I.H. & Arculus, R.J. (2013). Platinum-alloy and sulfur saturation in an arc-related basalt to rhyolite suite: Evidence from the Pual Ridge, eastern Manus Basin. *Geochimica et Cosmochimica Acta* **101**, 76–95.

Paterson, D., de Jonge, M. D., Howard, D. L., Lewis, W., McKinlay, J., Starritt, A., Kusel, M., Ryan, C. G., Kirkham, R., Moorhead, G. & Siddons, D. P. (2011). *The X-ray Flurorescence Microscopy Beamline at the Australian Synchroton*. AIP Conference Proceedings, **1365**, 219-222.

Patino Douce, A.E. & Beard, J.S. (1995). Dehydration-melting of Biotite Gneiss and Quartz Amphibolite from 3 to 15 kbar. *Journal of Petrology* **36**, 707-738.

Peck D. C., Keays R. R. & Ford R. J. (1992). Direct crystallization of refractory platinum-group element alloys from boninitic magmas: evidence from western Tasmania. *Australian Journal of Earth Sciences* **39**, 373–387.

Prendergast, M. (2009). *Monts de Cristal Platinum Project, NW Gabon*. Geological report on exploration activities. Lonmin plc.

Puchtel, I.S. and Humayun, M. (2001) Platinum group element fractionation in a komatiitic basalt lava lake. Geochim. Cosmochim. Acta 65: 2979-2994.
Raedeke, L.D. (1982). *Petrogenesis of the Stillwater Complex*. Unpublished PhD thesis, University of Washington, Seattle, 212p.

Rankenburg, K., Lassiter, J.C. & Brey, G. (2004). Origin of megacrysts in volcanic rocks of the Cameroon volcanic chain – constraints on magma genesis and crustal contamination. *Contributions to Mineralogy and Petrology* **147**, 129-144.

Rehkamper, M., Halliday, A.N., Fitton, J.G., Lee, D.-C., Wieneke, M., & Arndt, N.T. (1999). Ir, Ru, Pt and Pd in basalts and komatiites: New constraints for the geochemical behavior of the platinum group elements in the mantle. Geochimica et Cosmochimica Acta 63, 3915-3934.

Richard, P., Shimizu, N. & Allègre, C.J. (1976). 143Nd/146Nd, a natural tracer: an application to oceanic basalts, *Earth and Planetary Science Letters* **31**, 269–278.

Rollinson HR (2013) Using geochemical data: evaluation, presentation, interpretation, Routledge, Oxon, UK.

Rudnick, R.L. & Fountain, D.M. (1995). Nature and composition of the continental crust: A lower crustal perspective. *Reviews in Geophysics* **33**, 267–309.

Ryan, C., Kirkham, R., Hough, R., Moorhead, G., Siddons, D., de Jonge, M., Paterson, D., De Geronimo, G., Howard, D. & Cleverley, J. (2010a), Elemental X-ray imaging using the Maia detector array: The benefits and challenges of large solid-angle: *Nuclear*

Instruments & Methods in Physics Research, Section A–Accelerators, Spectrometers, Detectors and Associated Equipment **619**, 37-43.

Ryan, C., Kirkham, R., Siddons, D., Dunn, P., Laird, J., Kuczewski, A., Moorhead, G., De Geronimo, G., Davey, P., Jensen, M., Paterson, D., de Jonge, M., Howard, D. & Hough, R. (2010b). The Maia 384 detector array in a nuclear microprobe: A platform for high definition PIXE elemental imaging: *Nuclear Instruments & Methods in Physics* Research Section B-Beam Interactions with Materials and Atoms **268**, 1899-1902.

Ryan, C. G. (2000). Quantitative Trace Element Imaging using PIXE and the Nuclear Microprobe. *International Journal of Imaging Systems and Technology* **11**, 219-230.

Ryan, C.G., Siddons, D.P., Kirkham, R., Li, Z.Y., de Jonge, M.D., Paterson, D.J., Cleverley, J.S., Kuczewski, A., Dunn, P.A., Jensen, M., De Geronimo, G., Howard, D.L., Godel, B., Dyl, K.A., Fisher, L.A., Hough, R.M., Barnes, S.J., Bland, P.A., Moorhead, G.F., James, S.A., Spiers, K.M., Falkenberg, G., U , Boesenberg, U., Wellenreuther, G., (2014). The Maia detector array and x-ray fluorescence imaging system: locating rare precious metal phases in complex samples Proc. SPIE 8851, X-Ray Nanoimaging: Instruments and Methods 8851, 88510Q.

Ryan, C. G., Siddons, D. P., Kirkham, R., Dunn, P. A., Kuczewski, A., Moorhead, G., De Geronimo, G., Paterson, D. J., de Jonge, M. D., Hough, R. M., Lintern, M. J., Hoard, D. L., Kappen, P. & Cleverley, J. (2010c). The New Maia Detector System: *Methods for High Definition Trace Element Imaging of Natural Material*, in Denecke, M. A., and Walker, C. T., eds., *X-Ray Optics and Microanalysis*, **1221**, 9-17.

Sobolev S.V., Sobolev, A.V., Kuzmin D.V., Krivolutskaya, N.A., Petrunin, A.G., Arndt, N.T., Radko, V.A., & Vasiliev, Y.R. (2011). Linking mantle plumes, large igneous provinces and environmental catastrophes. *Nature* **477**, 312-316.

Teigler, B. & Eales, H.V. (1996). *The lower and critical zones of the western limb of the Bushveld Complex, as indicated by the Nooitgedacht boreholes*. Geological Survey of South Africa Bulletin **111**, 126

Thompson, R.N. Morison, M.A., Dicken, A.P. & Hendry, G.L. (1983). *Continental flood basalts ... Archahnids rule OK?* In: Hawkesworth, C.J. and Norry, M.J. (eds.) *Continental basalts and mantle xenoliths*. Shiva Nantwich, 158-185.

Tomkins, A.G., Rebryna, K.C., Weinberg, R.F. & Schaefer, B.F. (2012). Magmatic Sulfide Formation by Reduction of Oxidized Arc Basalt. J Petrol., 53, 1537-1567.

Toplis, M.J. & Corgne, A. (2002). An experimental study of element partitioning between magnetite, clinopyroxene and iron-bearing silicate liquids with particular emphasis on vanadium. *Contributions to Mineralogy and Petrology* **144,** 22–37.

Wille, M., Kramers, J.D., Nägler, T.F., Beukes, N.J., Schröder, S., Meisel, T., Lacassie, J.B. & Voegelin, A.R. (2007). Evidence for a gradual rise of oxygen between 2.6 and 2.5 Gafrom Mo isotopes and Re-PGE signatures in shales. *Geochimica et Cosmochimica Acta* **71**, 2417–2435.

Wilson, A.H. (2012). A chill sequence to the Bushveld Complex: insight into the first stage of emplacement and implications for the parental magmas. *Journal of Petrology* **53**, 1123–1168

Wingate, M.T.D., Campbell, I.H., Compston, W., and Gibson, G.M., 1998, Ion microprobe U-Pb ages for Neoproterozoic basaltic magmatism in southcentral Australia and implications for the breakup of Rodinia: Precambrian Research, v. 87, p. 135–159.

Yang, S., Maier, W.D., Lahaye,Y. & O'Brien, H. (2013). Strontium isotope disequilibrium of plagioclase in the Upper Critical Zone of the Bushveld Complex:

evidence for mixing of crystal slurries. *Contributions to Mineralogy and Petrology*, DOI 10.1007/s00410-013-0903-4

FIGURES

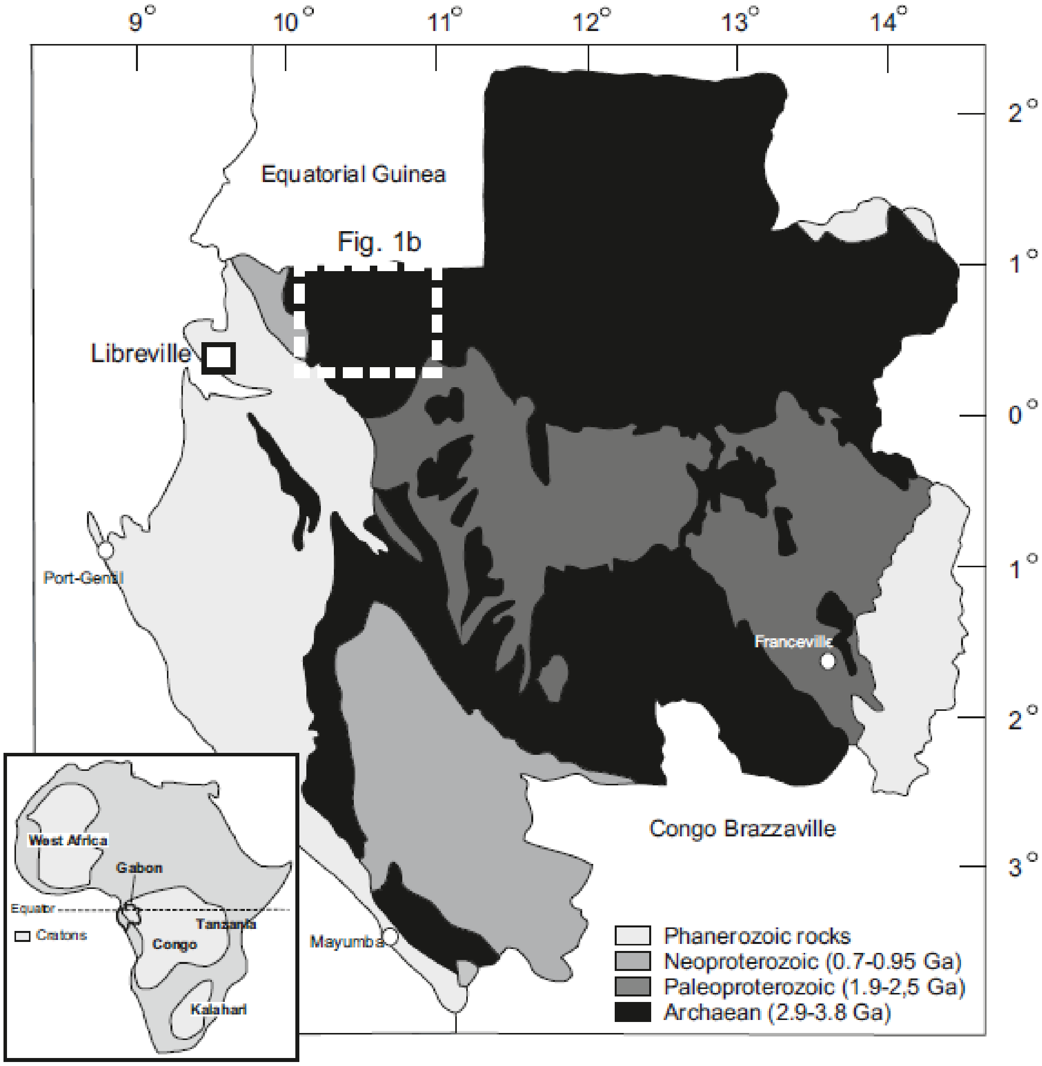

Fig. 1(a): Geological map of Gabon (modified after Chevalier et al. 2002). Insert shows segment enlarged in Fig. 1b. (b): Geological map of the Monts de Cristal Complex and its host rocks. Red line denotes outline of Monts de Cristal National Park. KG1-4 are individual blocks of Complex, and shaded areas with pink outline represent exploration focus areas. See insert of Fig. 1a for location.

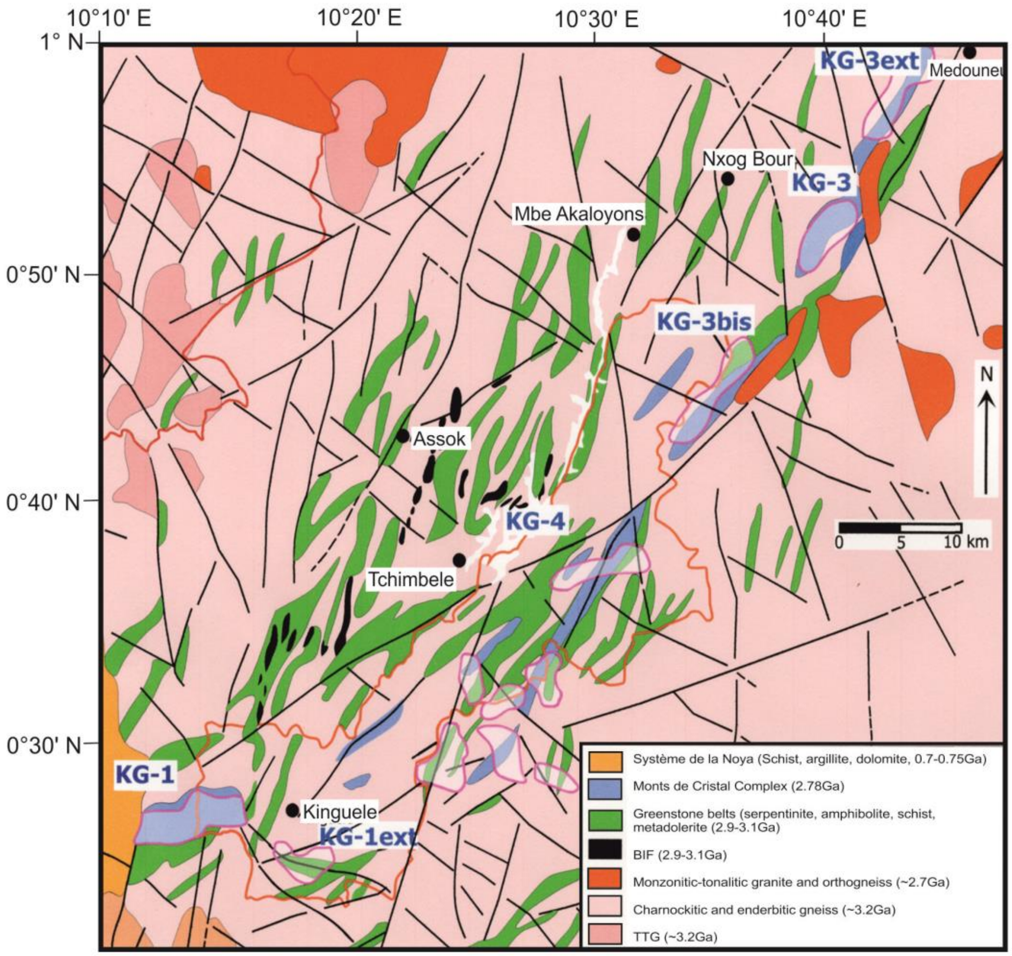

Fig. 2: Geological map of the KG1 body, showing sampling localities and drill core sites (denoted by stars, modified after Prendergast, 2009). Stippled line indicates a road. Coordinates are given in UTM system.

Fig. 3: Photomicrographs of Monts de Cristal rocks. (a) Olivine pyroxenite showing olivine inclusions in orthopyroxene. Sample Olpx21. (b) Orthopyroxene adcumulate, sample Px21. (c) Orthopyroxenite mesocumulate. Zoning is indicated by dark coronas along rims of grains. Sample Px18. (d) Chromite clusters within orthopyroxene of orthopyroxenite adcumulate. Sample Px21. (e) Chromite clusters within altered inclusion in orthopyroxene. Sample Px21. (f) Norite, showing euhedral and subhedral orthopyroxene as well as cumulus and intercumulus plagioclase. Sample Px16. (g) Olivine gabbro, showing intercumulus olivine and clinopyroxene as well as acicular plagioclase crystals. Sample Dy18. (h) Olivine gabbro, showing large euhedral clinopyroxene oikocryst containing plagioclase chadacrysts. Sample Dy18. Length of scale bar in each panel is 1mm.

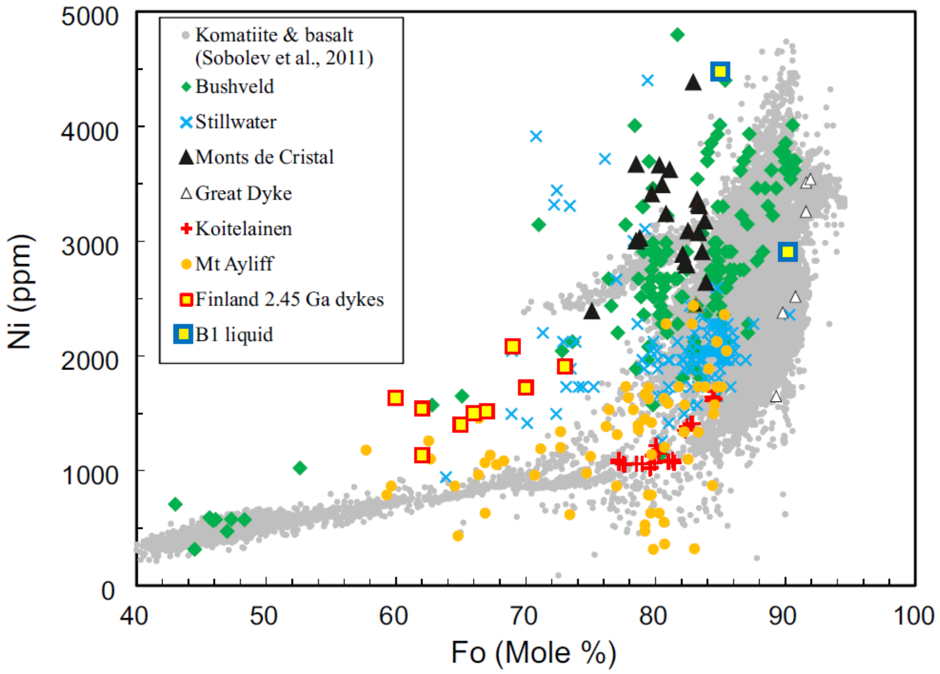

Fig. 4: Binary plot showing the variation of Fo and Ni contents of olivine in a number of layered intrusions. Note that the Monts de Cristal olivines have relatively high Ni contents compared to other intrusions with comparable Fo contents. Bushveld data are from Teigler and Eales (1996), Maier and Eales (1997) and Wilson (2012), Great Dyke data are from Wilson (pers. com., 2012), Koitelainen data are from Hanski (unpublished, pers. com., 2013), Stillwater data are from Raedeke (1982) and Barnes and Naldrett (1986), Mt Ayliff data are from Lightfoot and Naldrett (1983) and Lightfoot et al. (1984), and Finnish dykes are unpublished data of Fangfang Guo. Data for global komatiites and basalts are from Sobolev et al. (2011).

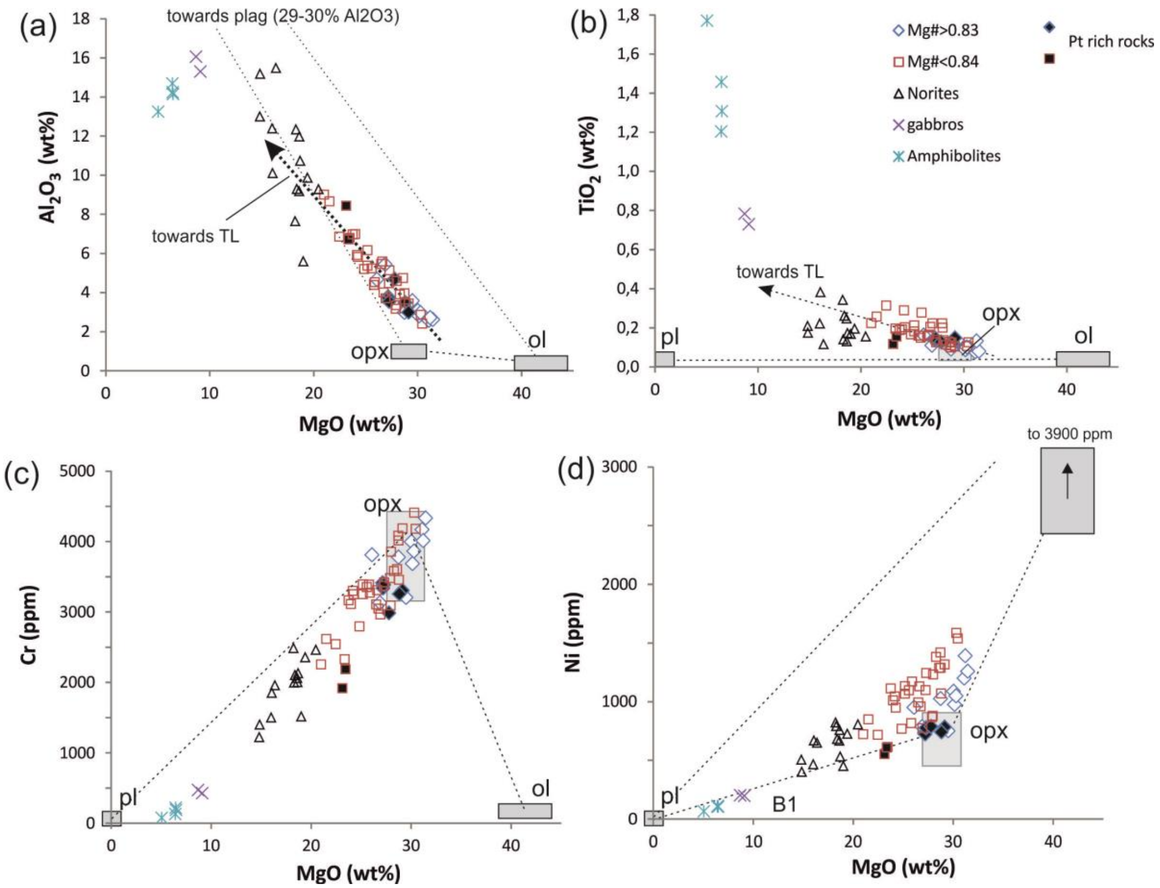

Fig. 5: Binary variation diagrams of (a) Al_2O_3, (b) TiO_2, (c) Cr, and (d) Ni, plotted vs MgO. Stippled arrows represent best fit lines through orthopyroxenites. Boxes linked by tielines indicate compositional ranges in analysed minerals.

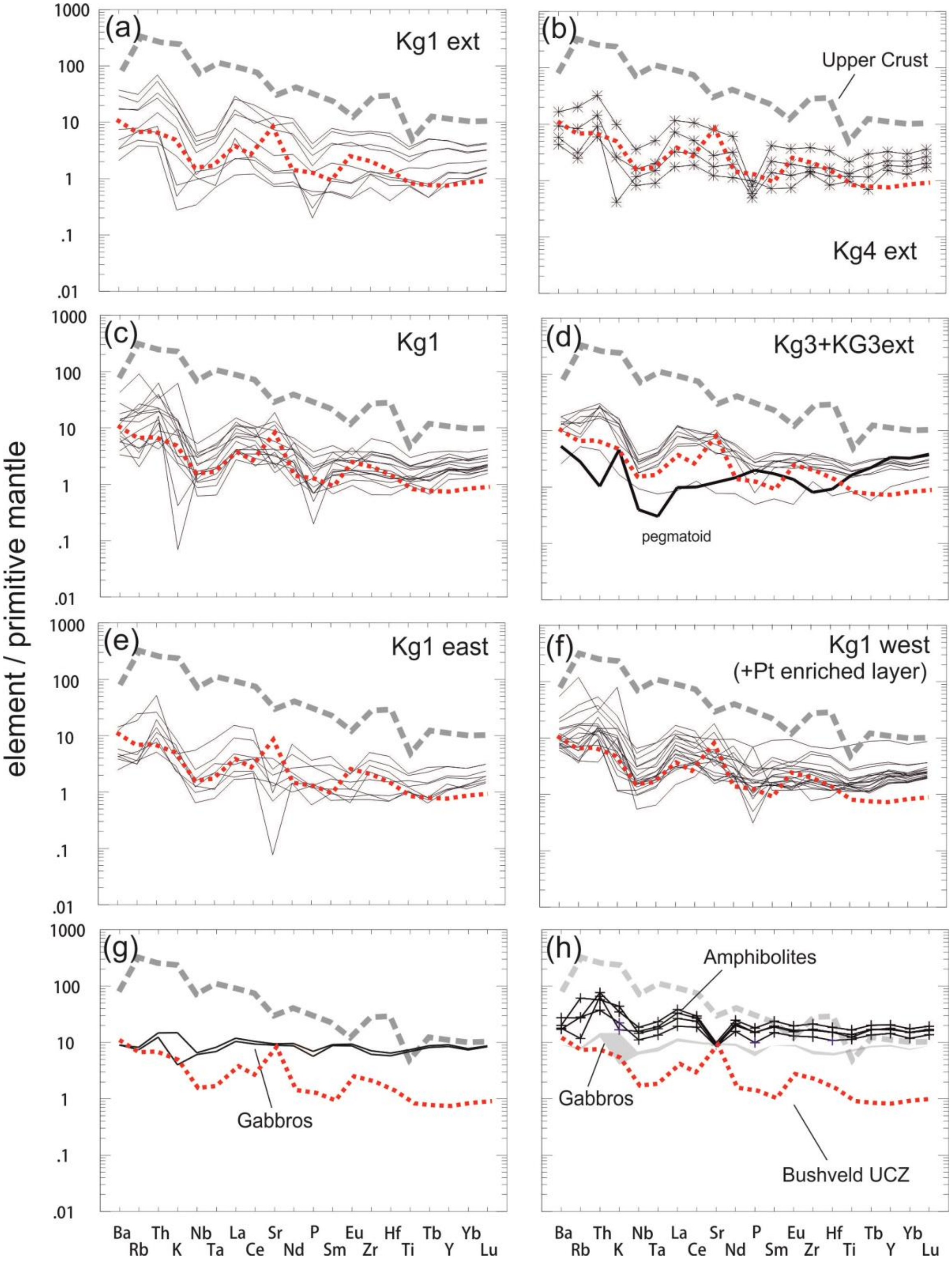

Fig. 6: Multi-element variation diagrams of lithophile trace elements. Data for Bushveld Upper Critical Zone are from Maier et al. (2013), and average Upper Crust is from Rudnick and Fountain (1995). Normalisation factors from McDonough and Sun (1995).

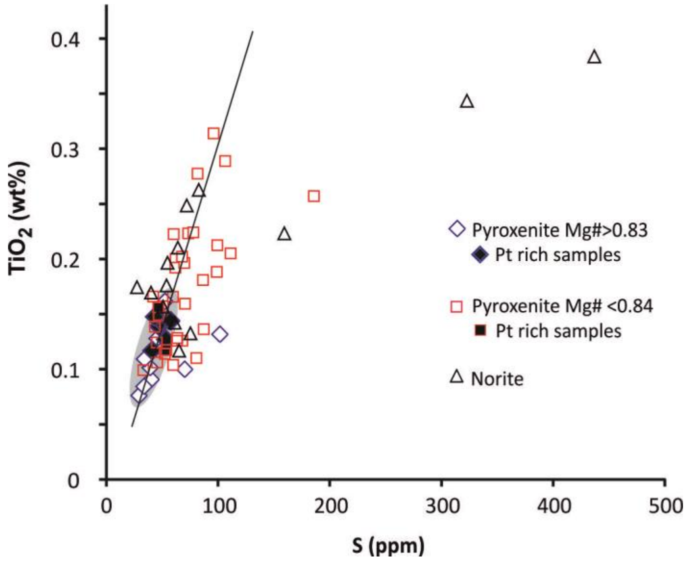

Fig. 7: Binary variation diagram of TiO_2 vs S. Regression line drawn through primitive orthopyroxenites (grey field, with exception of 2 samples) passes through origin and indicates approximately 100-150 ppm S in the putative trapped liquid at 0.4-0.5% TiO_2.

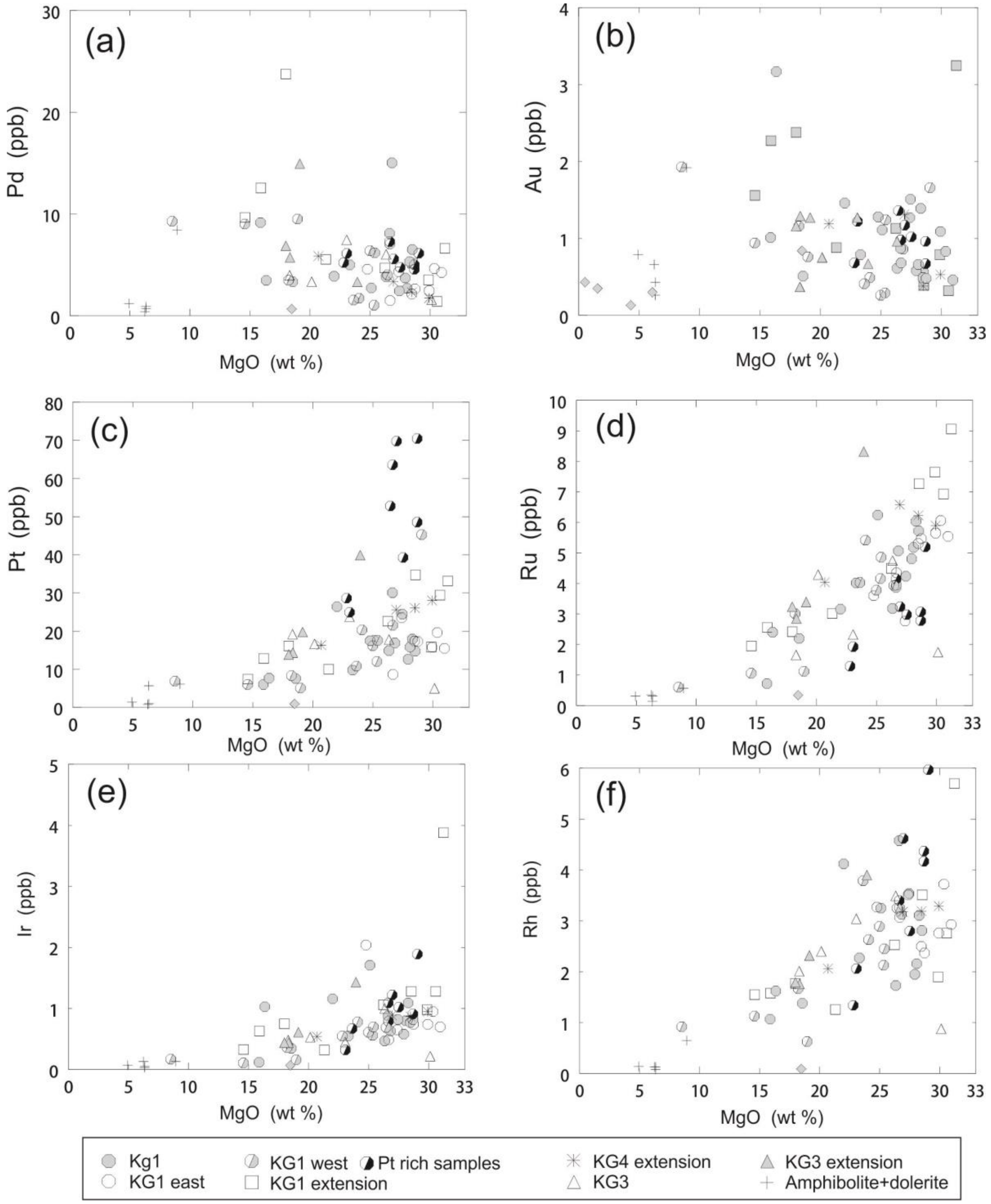

Fig. 8: Binary variation diagrams of chalcophile metals in various blocks of the Monts de Cristal Complex, plotted vs MgO. (a) Pd, (b) Au, (c) Pt, (d) Ru, (e) Ir, (f) Rh. Note negative correlations with MgO for Pd and Au, but positive correlations for Pt, Ru, Ir and Rh. See text for discussion.

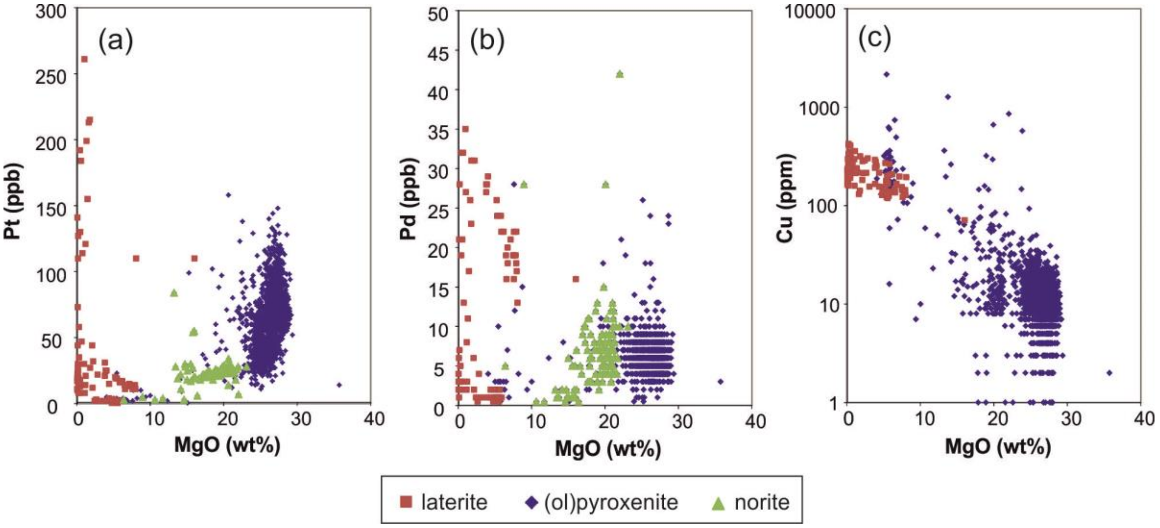

Fig. 9: Analyses of drill core samples plotted in binary variation diagrams vs MgO of (a) Pt, (b) Pd, and (c) Cu.

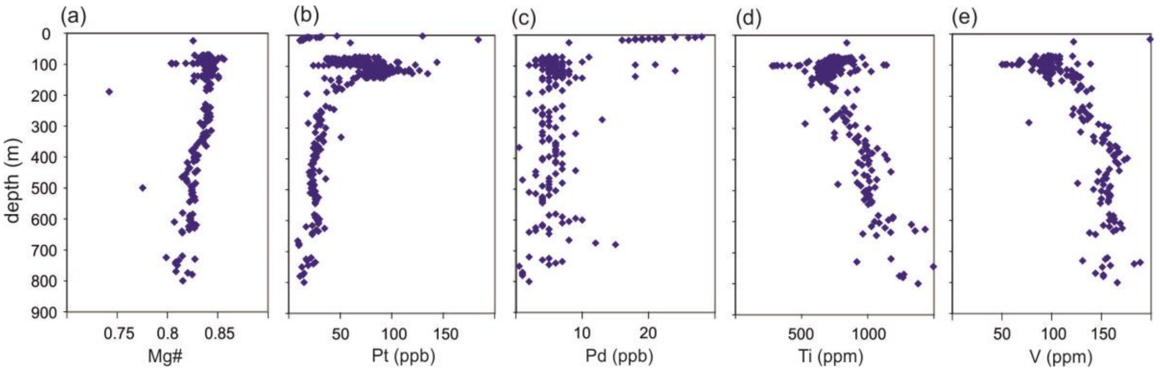

Fig. 10: Chemical data for drill core MPD-005

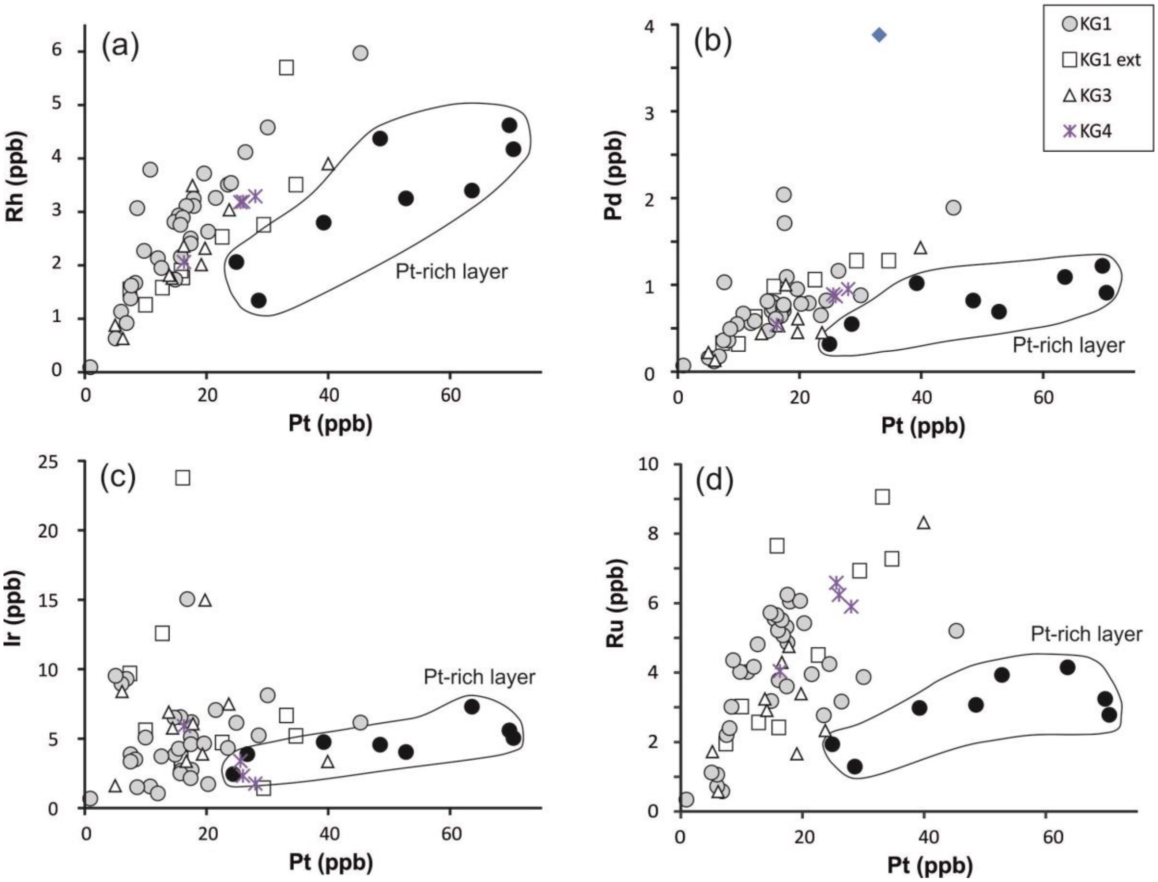

Fig. 11: (a-d) Binary variation diagrams for PGE. Note poor correlation between Pt and Pd, and high Pt/Pd ratios of most rocks. Outlined fields mark samples from Pt rich layer at KG1 west.

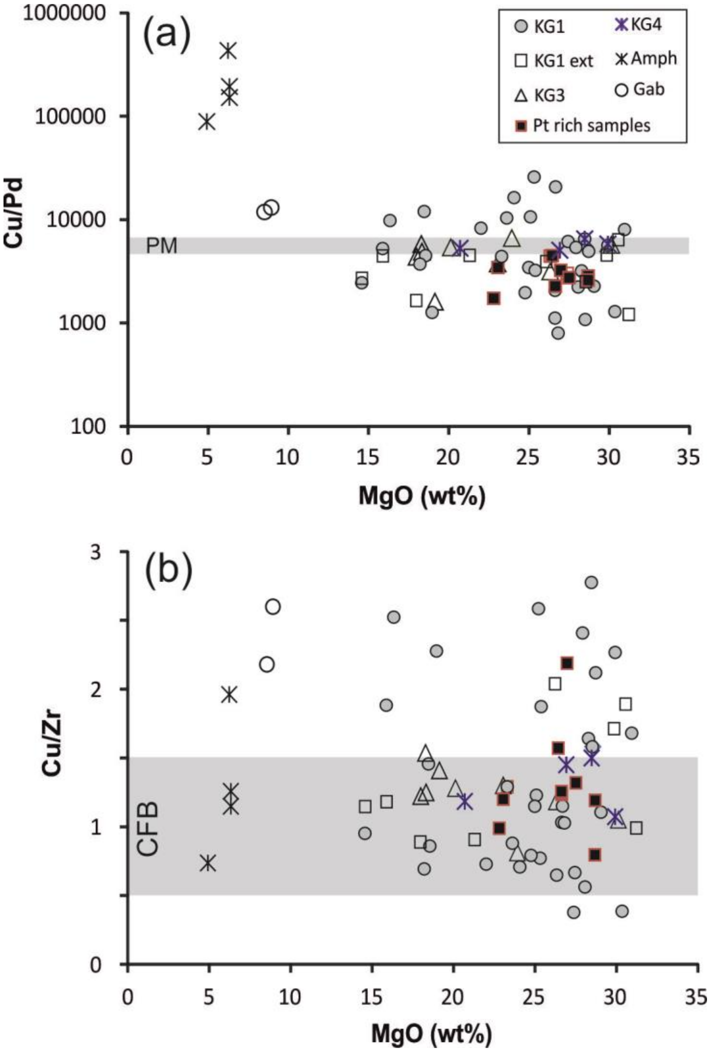

Fig. 12: Cu/Pd and Cu/Zr of Monts de Cristal rocks. Primitive mantle (PM) estimate is from Barnes and Maier (1999). Shaded bar in (b) represents range of South African continental flood basalts (CFB, from Maier et al., 2003).

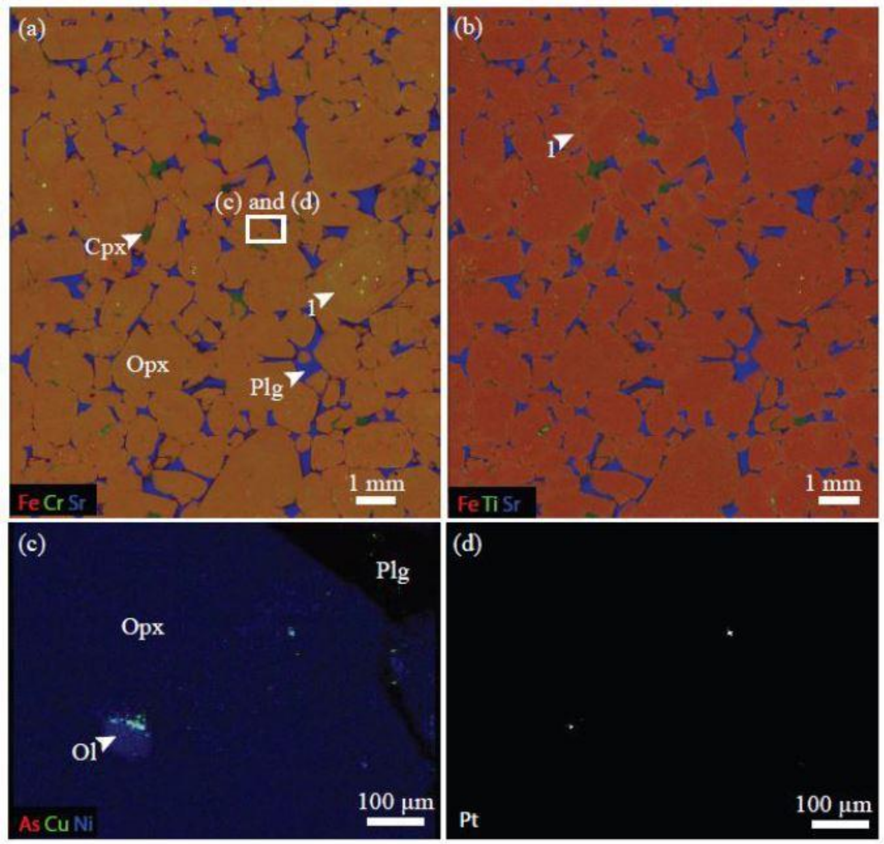

Fig. 13: a) and b) – three element false-colour RGB images of sample Px21. Each element is scaled to maximum values; Cr and Ti values are log transformed to enhance the compositonal range within the silicate phases. Note heterdacumulate texture of plagioclase oikocrysts (blue on both images) interstitial to orthopyroxene with minor intercumulus clinopyroxene (green on both images). Also note subtle complex internal zoning in Cr in some grains (grain 1 in image a) and fine rims of elevated Ti in image b in areas outside the plagioclase oikocrysts (point 1 in image b). Light green highlights on both images are small chromite inclusions, preferentially located in grains showing Cr zoning. (c) Three element image for As (red) – Cu (green) and Ni (blue) – light green areas indicate probable presence of Cu-Ni rich sulphide. One of these sulfide areas occupies the grain boundary between opx host and an olivine inclusion. Pt peaks in (d) correspond to coincident highs for As, within areas enriched in Cu and Ni, but not exactly matching Cu-Ni peaks. Pt corresponds exactly to As peak in each case. Note also presence of isolated small Cu-rich phases, probably sulphide, with no associated Pt or As, at opx margin.

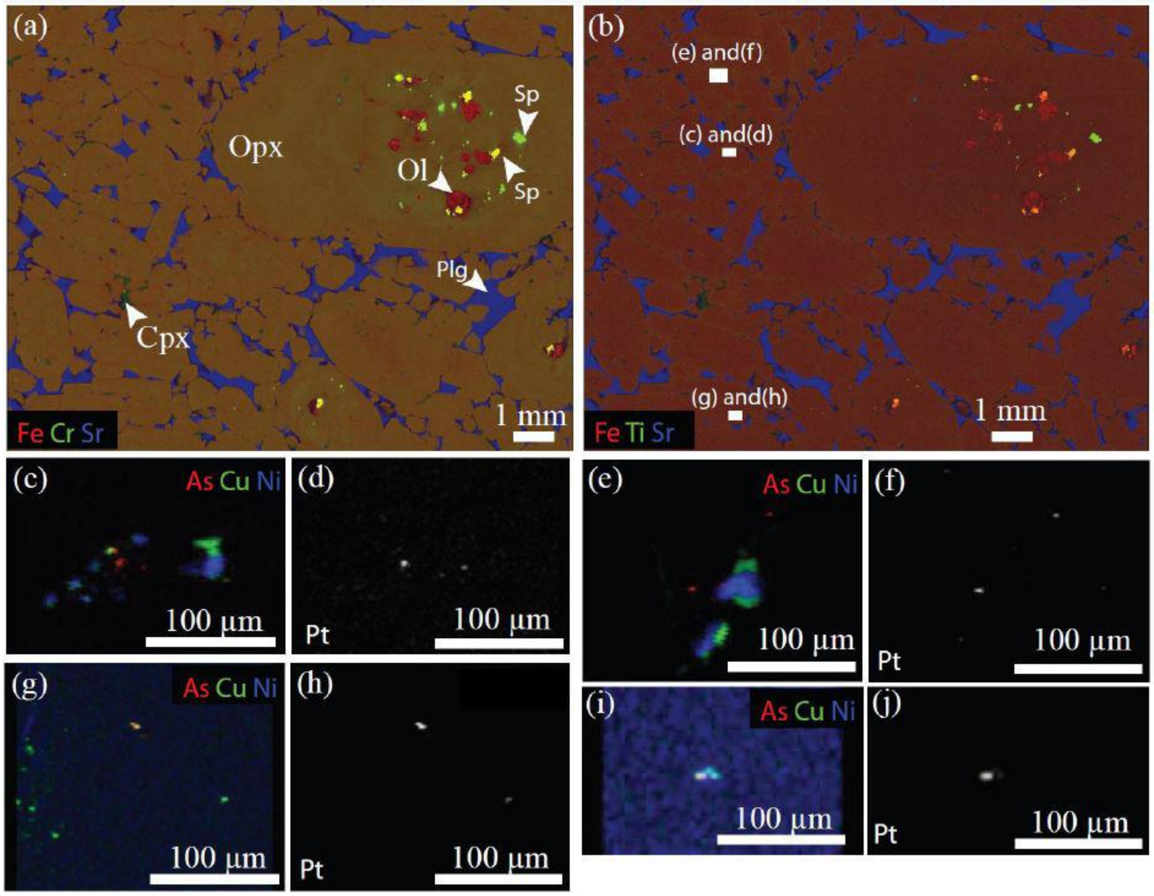

Fig. 14: Sample Px17A, with same combinations of elements as in Fig. 13a. Note abundant inclusions of olivine (red) and chromite (green) in Cr-zoned opx. No Pt grains were found in this grain, however. Enlarged areas show As-Cu-Ni three element maps as above, and corresponding single-element concentration maps for Pt. Note in all areas that Pt hits are associated with areas containing all three elements As, Cu and Ni, but the Pt peaks are very specifically associated with As, and do not necessarily occur directly within what appear to be sulphide aggregates. These aggregates are all occurring at or indistinguishably close to opx grain boundaries, but with no systematic relationship to plag oikocrysts.

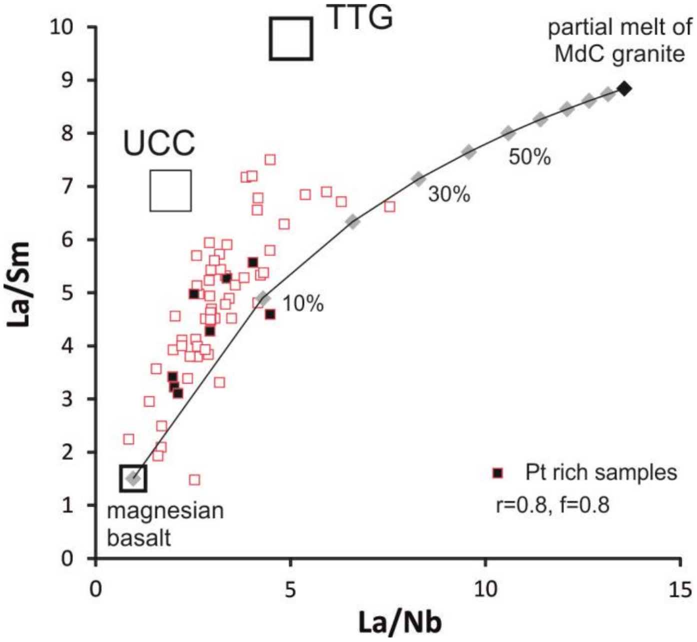

Fig. 15: Plot of La/Sm vs La/Nb for MdC rocks. Also plotted is average upper continental crust (Rudnick and Fountain, 1995) and average 3.0-3.5 Ga TTG (Martin et al., 2005). Solid line represents mixing line between magnesian basalt and a contaminated magma produced by AFC (r=0.8, f=0.8) of magnesian basalt with a 17% partial melt of MdC country rock granite. Trace element contents of magnesian basalt are assumed to be 4x that of primitive mantle (PM), with PM data taken from McDonough and Sun (1995). See text for further discussion.